Author/s:
Saurav, Tanvir Mahmud

Title:
Effect of solidity on momentum and heat transfer of rough-wall turbulent flows

Date:
2020

Persistent Link:
https://hdl.handle.net/11343/267999

Effect of solidity on momentum and heat transfer of rough-wall turbulent flows

Tanvir Mahmud Saurav

ORCID: 0000-0002-7258-2818

Submitted in total fulfilment of the requirements of the degree of

Master of Philosophy

Department of Mechanical Engineering
The University of Melbourne

October 2020

Produced on archival quality paper.

Abstract

A major area of interest in engineering is the skin-friction drag and convective heat transfer of surfaces in turbulent flow, such as turbine blades, marine vehicles, and airplanes. While these surfaces may appear smooth, they almost always have some form of roughness, for example, pitting on the surface of a turbine blade, barnacles on the hull of a marine vehicle, or rivets on the wings of an airplane. For a given roughness and flow speed, the Moody diagram can be used to find the frictional drag or pressure drop. A similar diagram can be constructed to find heat transfer. Although widely used, the biggest limitation of the Moody diagram is that the Nikuradse equivalent sand grain roughness has to be known for the rough surface in question. Another limitation of the Moody diagram is in predicting skin friction for transitionally rough surfaces, owing to the unrepresentative Colebrook fit. Also, while the effects of varying key roughness topographical parameters on momentum transfer have been studied extensively, relatively little is known on heat transfer. Over the years, researchers have used computational and experimental methods to investigate the flows over a number of roughness types. This thesis expands on the computational works on sinusoidal roughness by systematically investigating the effect of varying roughness solidity on both momentum and heat transfer in turbulent air flow, and the underlying flow physics that give rise to the observed behaviour. Rough-wall flows transfer more momentum and heat when compared to smooth-wall flows, and it is found that an increase in solidity for a matched equivalent sand-grain roughness height causes a greater increase in heat transfer than the increase in momentum transfer due to increased wetted area and increased recirculation region that facilitates mixing.

Declaration

This is to certify that

1. the thesis comprises only my original work towards the MPhil,
2. due acknowledgement has been made in the text to all other material used,
3. the thesis is less than 50,000 words in length, exclusive of tables, maps, bibliographies and appendices.

Tanvir Mahmud Saurav, October 2020

Acknowledgements

I would like to express my sincere gratitude to my supervisors, Dr. Daniel Chung and Dr. Nicholas Hutchins, for giving me the opportunity to start my journey as a researcher. Thank you for your patience, motivation, and your immense knowledge that helped me navigate these deep waters of fluid dynamics research. Without your guidance and persistent help, this dissertation would not have been possible.

I would also like to thank my committee members, Dr. Jason Monty and Dr. Simon Illingworth, for providing me with directions at times when I felt my progress has come to a halt. I could not have asked for a better committee.

To Dr. Thomas Jelly and Dr. Wagih Abu Rowin, thank you for the guidance in writing my dissertation and proofreading. Your expertise has not only helped me complete this dissertation but also develop a better understanding of fluid dynamics through our stimulating discussions in our meetings.

In addition, I would like to thank Dr. Amirreza Rouhi and Michael Xie for helping me out with the first steps in research when I embarked on my journey. You have been a tremendous help in developing my basic understanding of computational fluid dynamics. I would also like to thank Tony and Katie for their friendship, guidance, and all the fun that we had together.

I would also like to take this opportunity to thank my parents and my sister for supporting me at every step of the way. Special thanks to my wife, Nusrat Mehnaz, for supporting me from halfway across the world in finishing my journey. Finally, we can start *our* journey and build a life together.

This work is funded by The University of Melbourne through the Melbourne Research Scholarship. The computational time is provided by the Pawsey Supercomputing Center with funding from the Australian Government and the Government of Western Australia, and National Computational Infrastructure (NCI Australia), an NCRIS enabled capability supported by the Australian Government.

Contents

List of Figures

Chapter 1
Background and objectives

1.1 Application of rough wall-bounded turbulent flows

Fluid flow, the motion of liquids and gases, can be characterised as either laminar or turbulent. Considering that a fluid is composed of many fluid particles, when these particles move in a highly ordered fashion characterised by smooth layers, it is called laminar flow (Çengel & Cimbala, 2018). Turbulent flow, on the other hand, is characterised by random, chaotic motion of the fluid particles. Most practical flows are also bounded by walls, for example, fluid flow in a pipe or channel, or over a surface. To predict whether a flow is laminar or turbulent, a dimensionless quantity called the Reynolds number, Re, is often used (Reynolds, 1883). For a channel, the bulk Reynolds number is defined as,

$$Re_b = \frac{hU_b}{\nu} \tag{1.1}$$

where U_b ($\mathrm{m\,s^{-1}}$) is the bulk velocity (average velocity across a cross section of the flow) of the fluid, h (m) is the height of the channel, and ν ($\mathrm{m^2\,s^{-1}}$) is the kinematic viscosity of the fluid. A low Reynolds number means the flow is dominated by viscous forces, whereas a high Reynolds number means the flow is dominated by inertial forces. Experimentally it has been shown that in a pipe, laminar flow

occurs for $Re_b < 500$, and turbulent flow occurs for $Re_b \geq 2000$ (Schlichting, 1936). In most practical applications such as flow over the wings of an airplane, around turbine blades or ship hulls, or over large vegetation canopies, the velocity of the flow or the dimension of the surface is large such that Re is typically many orders of magnitude higher, and hence the flow is turbulent. This has made predicting wall-bounded turbulent flow a practical interest since the early days of pioneers such as Ludwig Prandtl and Theodore von Kármán. Two quantities are of particular interest in wall-bounded flows: skin-friction drag and heat transfer through the wall. A confounding issue is that not all walls are the same, and in fact, most practical surfaces also have some form of roughness. For example, the external surface of an airplane has roughness elements such as rivets, fairings, or weldings; in marine vehicles such as ships, the biofouling on the hull (Schultz *et al.*, 2011); and in natural flows, atmospheric flows over and within vegetation canopies (Raupach & Shaw, 1982; Raupach *et al.*, 1991; Thom, 1971), and over ocean waves (Yang *et al.*, 2013). Also in heat exchangers and in turbine blades, surface roughness plays a vital role in altering the flow characteristics (Webb & Eckert, 1972). Such surfaces typically generate greater skin friction and heat transfer than a smooth wall (Dipprey & Sabersky, 1963). Thus, a better understanding of turbulent flow over rough walls, and in particular, the effects of key roughness topographical parameters, can help build better airplanes, heat exchangers, and predict the weather and climate more accurately.

In this study, an open channel numerical setup is utilised and the flow is taken to be incompressible. Real-life conditions are often different: roughness topography is generally not homogeneous, curvature introduces pressure gradient effects in turbomachinery flows, and the flow may also be compressible. However, the homo-

geneous roughness topography in this study is varied in a systematic manner, with an aim to provide a general understanding of how certain roughness parameters affect momentum and heat transfer.

1.2 Rough-wall drag and heat transfer

Because of the practical implications of turbulent skin-friction drag and heat transfer through the wall, engineers want to know these quantities for a given surface, fluid properties, and flow conditions. In the case of an open channel (Figure 1.1), the skin-friction drag can be written as a function:

$$\frac{\tau_w}{\rho} = \frac{\tau_w}{\rho}(U_b, \nu, k, h) \tag{1.2}$$

where τ_w ($\mathrm{kg\,m^{-1}\,s^{-2}}$) is the wall shear stress and ρ ($\mathrm{kg\,m^{-3}}$) is the density of the fluid. k (m) can be any measure of roughness, for example, peak-to-trough roughness height, mean roughness height, root mean square height, etc. Here, the right-hand side quantities are the observables (input of the function), and the left-hand side is the desired output. In a similar fashion, the heat flux through the wall can be written as

$$\frac{q_w}{\rho c_p} = \frac{q_w}{\rho c_p}(U_b, \nu, k, h, \alpha, \Theta_m) \tag{1.3}$$

where q_w ($\mathrm{kg\,s^{-3}}$) is the heat transfer through the wall, c_p ($\mathrm{m^2\,s^{-2}\,K^{-1}}$) is the specific heat at constant pressure, α ($\mathrm{m^2\,s^{-1}}$) is the thermal diffusivity, and,

$$\Theta_m \equiv \frac{\int_0^h U(\Theta - \Theta_w)\,\mathrm{d}z}{\int_0^h U\,\mathrm{d}z} \tag{1.4}$$

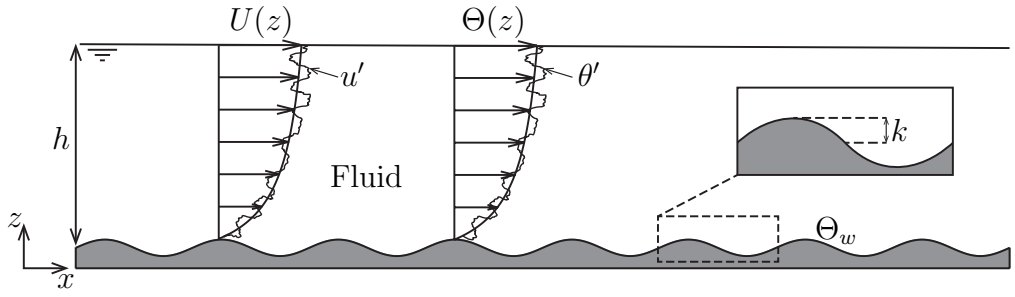

Figure 1.1: 2-D representation of an open channel with height, h, with flow towards the positive x-direction. The schematic represents an incompressible flow with no buoyancy stratification. The bottom stationary wall is rough with a roughness height, k, and temperature Θ_w. The mean velocity and temperature profiles are $U(z)$ and $\Theta(z)$ respectively, with instantaneous fluctuation u' and θ' about the mean.

(K) is the mixed-mean temperature, defined as the average temperature flowing through the cross-section of the channel (Owen & Thomson, 1963; Pirozzoli *et al.*, 2016). Here, U ($\mathrm{m\,s^{-1}}$) and Θ (K) are the mean velocity and temperature of the fluid, respectively, and z is the wall-normal direction. Using Buckingham's π Theorem, these variables can be used to obtain dimensionless groups. Because there are two (length and time) primary dimensions and five variables for τ_w/ρ (1.2), and three (length, time, and temperature) primary dimensions and seven variables for $q_w/(\rho c_p)$ (1.3), it can be shown that there are $5-2=3$ and $7-3=4$ dimensionless groups for τ_w/ρ and $q_w/(\rho c_p)$ respectively. The roughness height can be non-dimensionalised as relative roughness k/h. Also, U_b, ν, and h can be combined to create the bulk Reynolds number, $Re_b = hU_b/\nu$ (1.1). α and ν can also be combined to form another non-dimensional term known as Prandtl number, defined as $Pr = \nu/\alpha$. Thus, dimensional analysis leads to the following reduced form for skin friction and heat transfer:

$$\frac{\tau_w}{\frac{1}{2}\rho U_b^2} \equiv C_f \equiv C_f\left(Re_b, \frac{k}{h}\right) \tag{1.5}$$

$$\frac{q_w}{\rho c_p U_b \Theta_m} \equiv St \equiv St\left(Re_b, \frac{k}{h}, Pr\right) \tag{1.6}$$

Here, C_f is called the skin friction coefficient and St is the heat transfer coefficient called the Stanton number. C_f is the ratio of the wall shear stress to the dynamic pressure, while St is the ratio of the heat transferred into or from the fluid to the thermal capacity of the flowing fluid.

If the equivalent sand-grain roughness height, k_s (explained in Section 1.7), of the rough surface and bulk Reynolds number of the flow are known (i.e. k_s/k is a known value), the Moody diagram (Moody, 1944) in Figure 1.2 can be used to find the skin friction of a surface. The Moody diagram, based on the original experiment of Nikuradse (1933) and Colebrook (1939) (explained in Section 1.7) is a graphical representation of (1.5), and is a tool to find pressure drop in pipe flows. Similarly, a Stanton number plot (Figure 1.4) can be used to find the heat flux through the wall. The prerequisite is, of course, to solve the flow and find the equivalent sand-grain roughness, k_s/k. However, even with known k_s/k, there are some limitations to finding the skin friction or heat flux, as explained further in Section 1.7. Before the advent of high-performance computing, tedious experiments were the only ways to investigate the effects of surface roughness. However, with the progress of numerical methods and computational power, this process can now also be done by numerically solving the Navier–Stokes equations and the passive scalar transport equation.

1.3 Navier–Stokes equations and boundary conditions

The following discusses the governing equations for fluid motion and forced convective heat transfer. Note that it is assumed that the temperature does not affect the fluid properties such as density and viscosity, and hence it is considered a passive scalar. This is a reasonable approximation when buoyancy forces are small compared to inertial forces, and when temperature variations are small compared to the absolute temperature. For an incompressible flow, the governing equations can be expressed as

$$\frac{\partial u_i}{\partial x_i} = 0 \tag{1.7}$$

$$\frac{\partial u_i}{\partial t} + \frac{\partial u_i u_j}{\partial x_j} = -\frac{1}{\rho}\frac{\partial p}{\partial x_i} + \nu\frac{\partial^2 u_i}{\partial x_j^2} + F_i \tag{1.8}$$

$$\frac{\partial \theta}{\partial t} + \frac{\partial u_i \theta}{\partial x_i} = \alpha\frac{\partial^2 \theta}{\partial x_i^2} + G \tag{1.9}$$

Here, $\{x_1, x_2, x_3\} = \{x, y, z\}$ are the streamwise, spanwise, and wall-normal directions. The corresponding velocity components are $\{u_1, u_2, u_3\} = \{u, v, w\}$ respectively, and t is the time. Also, $F_1 = -(1/\rho)\mathrm{d}P/\mathrm{d}x$, where $\mathrm{d}P/\mathrm{d}x < 0$ is the uniform, driving pressure gradient, $F_2 = F_3 = 0$, and $\partial p/\partial x_i$ is the periodic fluctuating pressure gradient. Note that F_1 is a body force, which can either be pressure gradient (for pipe or full channel flows) or due to gravity (for open channel flow). As for the passive scalar (temperature in this case) transport equation, the temperature is decomposed into a mean, $T(x) = T_0 + (\mathrm{d}T/\mathrm{d}x)x$ where $\mathrm{d}T/\mathrm{d}x$ is a uniform and constant–in–time streamwise gradient of the temperature, and a periodic component θ such that the total temperature is given by $T_T = T_0 +$

$(\mathrm{d}T/\mathrm{d}x)x+\theta$. This streamwise gradient was introduced by Kawamura *et al.* (1998), and can either be positive (heating along the flow) or negative (cooling along the flow). $G = -u\,\mathrm{d}T/\mathrm{d}x$ is thus a driving term resulting from the mean temperature gradient supplied during the simulation, and the governing equation is solved for the periodic component, θ. For an open channel (Figure 1.1), the boundary conditions are taken to be periodic in the streamwise and spanwise direction, with no–slip–impermeable ($u = v = w = 0$) and free–slip–impermeable ($\partial u/\partial z = \partial v/\partial z = 0, w = 0$) boundary conditions imposed at the bottom wall and top respectively. The bottom wall has an isothermal boundary condition such that $\Theta_w = 0$. Thus, the true wall temperature is actually $T_w = T(x)+\Theta_w = T_0+(\mathrm{d}T/\mathrm{d}x)x+0$. The top surface is taken to be adiabatic, hence, $\partial\theta/\partial z = 0$. A constant heat-flux condition can also be imposed at the wall. However, this would force the breakdown of Reynolds analogy ($2S_t/C_f$) because at the wall, $\partial\theta/\partial z$ is defined for temperature but a no-slip condition is defined for velocity. The boundary conditions are kept consistent for both velocity and temperature as much as possible.

1.4 Laminar flow

For a fully developed laminar (i.e. parallel shear) flow that has reached steady state, the flow does not depend on t, and the first term on the left hand side of (1.8) drops out. Because laminar flow is parallel shear flow, $v = w = 0$, the pressure fluctuation p is zero, and the velocity is only a function of wall-normal direction, z, i.e. $u = u(z)$. By analytically solving (1.8), the velocity profile of such a flow can thus be obtained:

$$0 = \nu \frac{\partial^2 u}{\partial z^2} + F_1 \tag{1.10}$$

where $F_1 = -(1/\rho)\mathrm{d}P/\mathrm{d}x > 0$. Integrating this equation twice with respect to z and applying the boundary conditions at $z = 0$ to $z = h$, the expression for the velocity profile can be obtained as:

$$u(z) = h^2 \frac{F_1}{\nu} \left[\frac{z}{h} - \frac{1}{2} \frac{z^2}{h^2} \right] \tag{1.11}$$

Averaging (1.11) in the z-direction gives an analytical expression of the bulk velocity:

$$U_b = \frac{h^2}{3\nu} F_1 \tag{1.12}$$

Using (1.11) and (1.12), it can now be written as $u(z) = 3U_b[(z/h) - (1/2)(z/h)^2]$. In terms of U_b, F_1 can be written as $F_1 = 3\nu U_b/h^2$. The definition of wall shear stress for a smooth wall is given as:

$$\frac{\tau_w}{\rho} = \nu \left. \frac{\partial u}{\partial z} \right|_{z=0} \tag{1.13}$$

Differentiating 1.11 and using the definition of wall shear stress, it is obtained, $\tau_w = \rho h F_1$. From (1.5), it can be shown that $C_f = 6/Re_b$.

Following similar arguments of a fully developed flow at steady state, it can be said that for temperature, $\theta = \theta(z)$. Thus, from (1.9), it is obtained:

$$0 = \alpha \frac{\partial^2 \theta}{\partial z^2} + G \tag{1.14}$$

Because $G = -u\,\mathrm{d}T/\mathrm{d}x$, $u = 3U_b[(z/h) - (1/2)(z/h)^2]$ can be substituted. Now

integrating (1.14) in the z-direction twice and applying the boundary conditions, it can be written,

$$\theta(z) = \frac{h^2 U_b}{\alpha}\frac{\mathrm{d}T}{\mathrm{d}x}\left(\frac{z^3}{2h^3} - \frac{z^4}{8h^4} - \frac{z}{h}\right) \tag{1.15}$$

Using the definition of mixed mean temperature (1.4), it is found that $\Theta_m = -(17/35)(h^2 U_b/\alpha)(\mathrm{d}T/\mathrm{d}x)$. The heat flux through the wall is $q_w/(\rho c_p) = \alpha\,\partial\theta/\partial z|_{z=0}$. Differentiating (1.15) once and evaluating at $z = 0$, it is obtained, $\alpha\,\partial\theta/\partial z|_{z=0} = -hU_b\mathrm{d}T/\mathrm{d}x$. Using $Pr = \nu/\alpha$, (1.6) can be used to find that $St = (35/17)(Re_b^{-1}Pr^{-1})$.

1.5 Smooth-wall turbulent flows

Turbulent flows are inherently unsteady and spatially varying. The velocity components, pressure in a turbulent flow can be decomposed into a mean component and a fluctuating component, such that, $u = \bar{u} + u'$, $v = \bar{v} + v'$, $w = \bar{w} + w'$, $p = \bar{p} + p'$ and $\theta = \bar{\theta} + \theta'$ where the term $\bar{\cdot}$ indicates average in time and periodic wall-parallel directions x and y, and $\cdot'$ is the instantaneous fluctuating component. After substituting the decomposed quantities into the Navier–Stokes equation introduced earlier and then averaging, the Reynolds-averaged Navier–Stokes (RANS) equations can be derived. Considering the open channel in Figure 1.1, it can be written

$$0 = \nu\frac{\partial^2\bar{u}}{\partial z^2} - \frac{\partial\overline{u'w'}}{\partial z} + F_1 \tag{1.16}$$

$$0 = \alpha\frac{\partial^2\bar{\theta}}{\partial z^2} - \frac{\partial\overline{\theta'w'}}{\partial z} + G \tag{1.17}$$

The $\overline{u'w'}$, $\overline{\theta'w'}$ terms make the number of unknowns more than the total number

of equations. Thus, an analytical solution for turbulent flow is impossible, and the velocity and temperature profiles of turbulent flow do not have simple analytical expressions as that of laminar flow. Instead, they consist of multiple regions. Prandtl (1925), von Kármán (1930), and subsequently Milikan (1938) derived mathematical expressions for various regions of the mean velocity profile using what is essentially dimensional reasoning. The regions are mainly viscous sublayer, buffer layer, log-layer, and wake layer. Considering $\bar{u}$, it is dependent on the following parameters:

$$\bar{u} = \phi\left(z, \frac{\tau_w}{\rho}, \nu, h\right) \tag{1.18}$$

where τ_w/ρ has units of $\mathrm{m}^2\,\mathrm{s}^{-2}$. Because this is the unit of velocity squared, a friction velocity, u_τ, is defined. Hence, $\tau_w/\rho = u_\tau^2$. This velocity can be used to non-dimensionalise $\bar{u}$, and thus dimensional analysis yields,

$$\frac{\bar{u}}{u_\tau} = \phi\left(\frac{zu_\tau}{\nu}, \frac{z}{h}\right) \tag{1.19}$$

Viscosity is dominant near the wall. Hence, for $z \ll h$,

$$U^+ \equiv \frac{\bar{u}}{u_\tau} = M\left(\frac{zu_\tau}{\nu}\right) = M(z^+) \tag{1.20}$$

where, ν/u_τ is called the viscous length. Quantities with a '+' superscript are non-dimensionalised with ν and u_τ, for example, $z^+ = zu_\tau/\nu$. In the outer layer where $z \gg \nu/u_\tau$,

$$\frac{\bar{u}_h - \bar{u}}{u_\tau} = N\left(\frac{z}{h}\right) = N(\eta) \tag{1.21}$$

where, $\bar{u}_h$ is the channel-height velocity. In the region where $\nu/u_\tau \ll z \ll h$, the

gradients of both the equations above match. Hence, taking the derivative of (1.20) and (1.21) with respect to z,

$$\frac{1}{u_\tau}\frac{\mathrm{d}\bar{u}}{\mathrm{d}z} = \frac{u_\tau}{\nu}\frac{\mathrm{d}M}{\mathrm{d}z} \tag{1.22}$$

$$-\frac{1}{u_\tau}\frac{\mathrm{d}\bar{u}}{\mathrm{d}z} = \frac{1}{h}\frac{\mathrm{d}N}{\mathrm{d}z} \tag{1.23}$$

Multiplying both sides of these two functions by z and equating them, it is obtained, $z^+\mathrm{d}M/\mathrm{d}z = -\eta\mathrm{d}N/\mathrm{d}z$. Since these two unrelated functions are equal, they must be equal to a constant. This constant is $(1/\kappa)$, where κ is known as the von Kármán constant.

$$z^+\frac{\mathrm{d}M}{\mathrm{d}z} = -\eta\frac{\mathrm{d}N}{\mathrm{d}z} = \frac{1}{\kappa} \tag{1.24}$$

Integrating both of these equations with respect to z,

$$M(z^+) = \frac{\bar{u}}{u_\tau} = \frac{1}{\kappa}\log z^+ + A \tag{1.25}$$

$$N(\eta) = \frac{\bar{u}_h - \bar{u}}{u_\tau} = -\frac{1}{\kappa}\log z^+ + B \tag{1.26}$$

Near the channel height, the velocity profile deviates from the derived logarithmic behaviour, and this region is known as the wake. A composite velocity profile for turbulent flow can thus be constructed by also including the description of the wake region by Coles (1956).

$$U^+ = \bar{u}/u_\tau = \underbrace{\frac{1}{\kappa}\log z^+ + A}_{\text{log-layer}} \quad + \quad \underbrace{\frac{2\Pi}{\kappa}\sin^2\left(\frac{\pi}{2}\frac{z^+}{Re_\tau}\right)}_{\text{wake}} \tag{1.27}$$

where, $Re_\tau \equiv hu_\tau/\nu$ is called the friction Reynolds number. This composite profile holds above the buffer layer. Tennekes & Lumley (1972) suggests that it exists from $z^+ \gtrsim 30$, while Pope (2000) suggests that it exists from $z^+ \gtrsim 50$. Recent literature such as Marusic *et al.* (2013) suggest that the log-layer spans $3Re_\tau^{1/2} < z^+ < 0.15Re_\tau$. A is a coefficient that depends on whether the wall is smooth, or on the type of roughness. Nagib & Chauhan (2008) and Marusic *et al.* (2013) recommend different values of this constant, but typically $A \approx 5$ for a smooth wall.

As for heat transfer in smooth wall, very close to the wall ($z \ll h$), the temperature profile is linear, and can be expressed by,

$$\Theta^+ \equiv \frac{\bar{\theta}}{\theta_\tau} = Prz^+ \tag{1.28}$$

where, the temperature is non-dimensionalised using the friction temperature, $\theta_\tau \equiv q_w/(u_\tau \rho c_p)$. Previous as well as recent studies such as Kader (1981); Pirozzoli *et al.* (2016) have found the presence of a logarithmic region in the temperature profile, much like the velocity profile of a turbulent flow. Hence, the temperature profile of a rough wall can be written as,

$$\Theta^+ \equiv \frac{\bar{\theta}}{\theta_\tau} = \frac{1}{\kappa_\theta}\log(z^+) + A_\theta(Pr) \tag{1.29}$$

where, $A_\theta(Pr)$ is an offset that depends on the molecular Prandtl number, Pr, and $\kappa_\theta \approx \kappa/Pr_t \approx 0.46$. Here, Pr_t is the turbulent Prandtl number. Yaglom (1979); Pirozzoli *et al.* (2016) have suggested values ranging from $0.85 - 0.9$ for Pr_t.

1.6 Rough-wall turbulent flows

For rough-wall flows, the mean velocity profile near the wall changes, resulting in a change of the skin-friction coefficient (Jiménez, 2004; Flack & Schultz, 2010, 2014). The change in the mean velocity profile can be characterised by a parallel downward shift, $\Delta U^+(k^+)$, from the smooth wall mean velocity profile, known as the roughness function (Hama, 1954). Thus, the velocity profile now becomes,

$$U^+ = \frac{1}{\kappa}\log z^+ + A - \Delta U^+(k^+) \tag{1.30}$$

The roughness function itself depends on the roughness Reynolds number, $k^+ = ku_\tau/\nu$, where k is a physical measure of the roughness height. Townsend (1976), in his outer layer similarity hypothesis, states that the flow is essentially the same above $z \gg k$ and $z \gg \nu/u_\tau$. Hence, a similar behaviour like the downward shift of a rough wall velocity profile from smooth wall profile should happen in case of temperature too (Yaglom, 1979). The temperature profile of a rough wall can be thought of as a parallel downward shift from the smooth wall temperature profile and can be written as a difference (MacDonald *et al.*, 2019):

$$\Theta^+ = \frac{1}{\kappa_\theta}\log(z^+) + A_\theta(Pr) - \Delta\Theta^+(k^+, Pr) \tag{1.31}$$

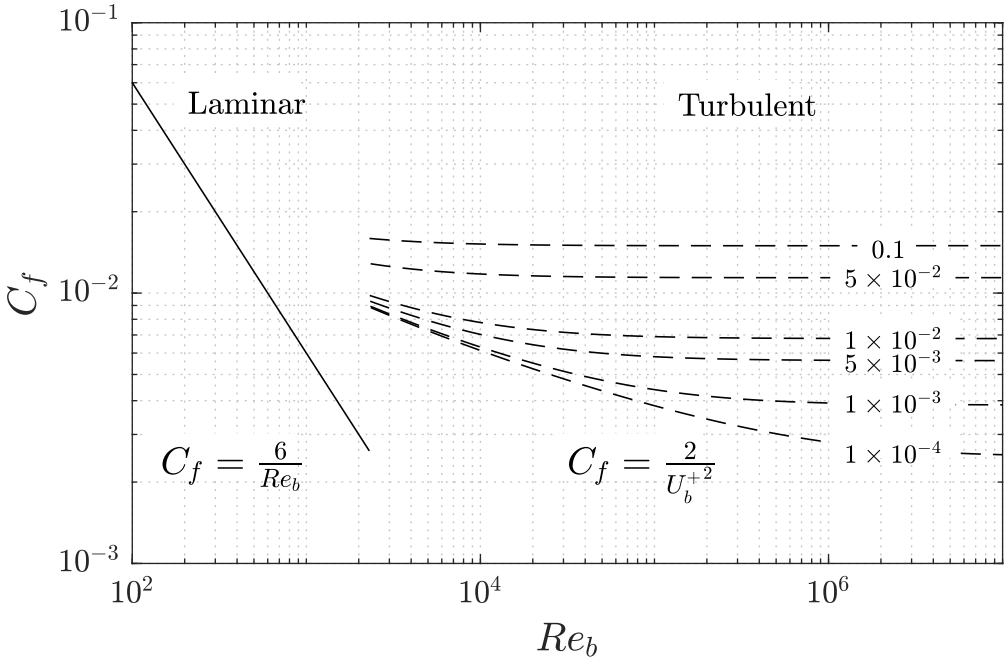

Figure 1.2: Moody chart: skin friction coefficient, C_f, against bulk Reynolds number, Re_b, for a range of relative roughness, k_s/h (labeled on each plot line), for fully developed open channel flow.

Nikuradse (1933) performed a wide range of experiments on pipes roughened with sand grains and calculated the pressure drop for different relative roughness heights. Colebrook (1939) later formulated an equation for the roughness function, which was subsequently used by Moody (1944) to calculate the Moody chart that engineers still use to predict the effect of surface roughness on the pressure or drag outcome. On the Moody chart (Figure 1.2), recreated for a fully developed open channel flow using the method of Moody (1944), the solid line on the left represents the skin-friction of a smooth-wall laminar flow for which an analytical solution of U_b and subsequently $C_f = 6/Re_b$ is possible (Section 1.4). At sufficiently high Reynolds number, the flow becomes turbulent. Because $\tau_w/\rho = u_\tau^2$, (1.5) gives us $C_f = 2/U_b^{+2}$ (U_b^+ is calculated numerically from (1.30)), and the Moody diagram

shows that the skin-friction coefficient for turbulent flow over a smooth-wall decreases with increasing bulk Reynolds number, Re_b. For low Reynolds number, the roughness elements can be considered completely submerged in the viscous sublayer, where the total drag is dominantly viscous drag with little form drag (Schultz & Flack, 2009). With increasing Re_b, the skin-friction coefficient first decreases and then becomes horizontal where it no longer depends on Re_b. This is known as the "fully rough" regime, where the roughness elements protrude above the thin viscous sublayer, and the total drag is dominated by form drag (Schultz & Flack, 2009; Busse *et al.*, 2017). With increasing roughness height, the roughness function ΔU^+ increases. Nikuradse (1933) explained this increment from transitionally rough regime to fully rough regime to be sudden, as he observed that for the uniform sand-grain roughness he studied, the roughness function no longer existed below $k_s^+ \approx 4$ (Figure 1.3). Colebrook (1939), however, proposed a roughness function with a gradual transition, $\Delta U^+ = (1/\kappa)\log(1 + 0.26k_s^+)$ (Figure 1.3).

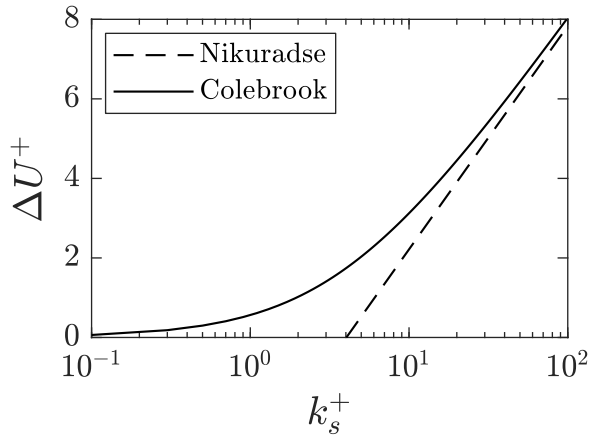

Figure 1.3: Roughness function, ΔU^+, against roughness height, k_s^+. Dashed line shows the fully rough asymptote of Nikuradse (1933), and solid line shows the relation found by Colebrook (1939).

As for the heat transfer, however, it does not have any component that is

comparable to the form drag component of skin friction (Owen & Thomson, 1963; Cebeci & Bradshaw, 1984). Heat transfer is controlled by the molecular property of the fluid and the transfer rate can never be greater than the conduction near the surface (Owen & Thomson, 1963). Figure 1.4 shows the heat transfer coefficient or Stanton number, St, against bulk Reynolds number, Re_b, constructed following Dipprey & Sabersky (1963), who proposed,

$$\Theta^+ = \frac{1}{\kappa_\theta}\log(z^+) + A_\theta - \Delta\Theta^+ \tag{1.32}$$

where, $\Delta\Theta^+ = b - A_\theta - (1/\kappa_\theta)\log(k_s^+)$, $b = 5.19(k_s^+)^{0.20}Pr^{0.44}$, and $A_\theta = 3.2$.

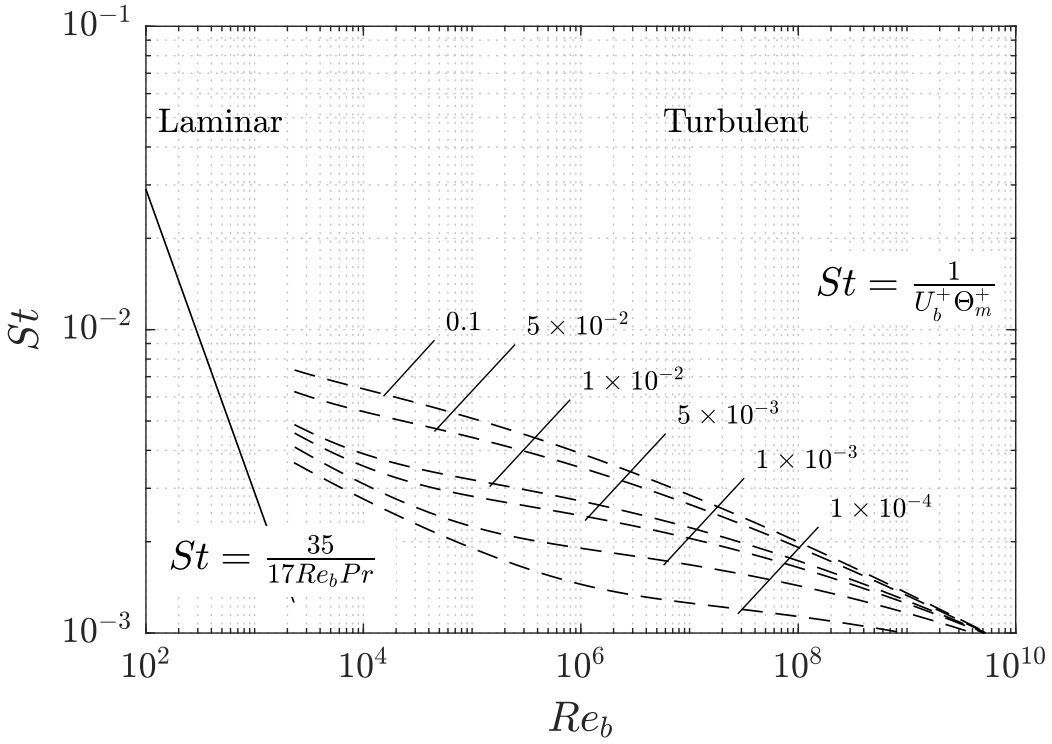

Figure 1.4: Stanton number, St, against bulk Reynolds number, Re_b, for $Pr = 0.71$ for a range of relative roughness, k_s/h (labeled on each plot line), for fully developed open channel flow.

From Figure 1.4, it can be seen that the heat transfer coefficient has an analytical expression $St = (35/17)(Re_b^{-1}Pr^{-1})$ when the flow is laminar. When the flow is turbulent, the Stanton number can be calculated from (1.6) as $St = 1/(U_b^+\Theta_m^+)$ using $q_w/(\rho c_p) = \theta_\tau u_\tau$, where both U_b^+ and Θ_m^+ are calculated numerically from (1.30) and (1.31). St increases in the transitionally rough regime, and Dipprey & Sabersky (1963) concluded that the heat transfer coefficient will peak at the end of the transitionally rough regime for a given roughness, and there is a limit for a combination of Reynolds number and Prandtl number beyond which St will not increase due to an increase in roughness.

To account for the numerous types of roughness encountered in practical situations, it is important to introduce a common parameter to characterise roughness types and their effects on the flow. Schlichting (1936) introduced the definition of frontal solidity, $\Lambda = S_f/S_p$, where S_f is the total frontal projected area of the roughness elements perpendicular to the flow direction, and S_p is the total plan area of the roughness elements parallel to the flow. Schlichting (1936) includes the frontal area of every roughness elements, irrespective of their mutual sheltering. Grimmond & Oke (1999) later found that such mutual sheltering starts to smoothen the roughness and reduces the drag, and later studies, such as Placidi & Ganapathisubramani (2015), only take into account the unsheltered roughness elements when calculating the frontal area. Musker (1980) and later Napoli *et al.* (2008) proposed a parameter called effective slope, ES. This is defined as,

$$ES = \frac{1}{L_x L_y}\int_0^{L_y}\int_0^{L_x}\left|\frac{\partial z_w(x,y)}{\partial x}\right|\mathrm{d}x\,\mathrm{d}y = 2\Lambda \tag{1.33}$$

where, z_w is the wall location, L_x is the streamwise length and L_y is the spanwise

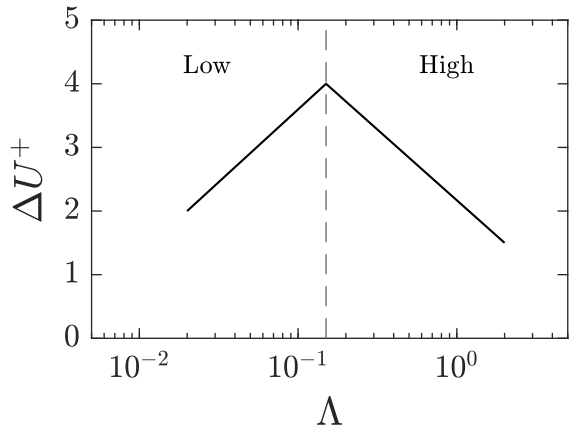

Figure 1.5: Sketch of roughness function, ΔU^+, against solidity, Λ, based on Jiménez (2004). Vertical line at $\Lambda = 0.15$ separates the low and high solidity regimes.

length of the surface. Thus, a flat wall has a solidity of $\Lambda = 0$, and for increasing values of solidity, the roughness becomes denser.

1.7 Motivations

1.7.1 Momentum transfer over rough walls

The measure of roughness, k_s, used in the formulation of roughness functions originally dates back to Nikuradse's equivalent sand grain roughness. The biggest limitation of the Moody diagram is that it is only accurate for surfaces with known k_s in the fully rough regime (Flack, 2018). This equivalent sand-grain roughness has to be determined numerically or experimentally and is not generic to all rough surfaces. Typically such numerical or experimental procedures are time and cost prohibitive as systematic studies need to be carried out for a given roughness height, k, until it reaches the fully rough regime, and then k_s/k has to be established. Also, the tran-

sitionally rough regime is not clearly understood as Flack & Schultz (2014) showed that the roughness effects are highly dependent on roughness geometry, such as solidity, anistropy, etc. Current understanding is that for low solidity ($\Lambda < 0.15$), the roughness function increases as solidity increases. Jiménez (2004); Flack & Schultz (2014) state that this increase happens due to an increased frontal area of the roughness. For high solidity ($\Lambda > 0.36$), the roughness function decreases as solidity increases (Figure 1.5). This is because of mutual sheltering of roughness elements (Grimmond & Oke, 1999; Jiménez, 2004).

1.7.2 Heat transfer over rough walls

Heat transfer over rough walls, especially the effect of varying roughness topographical parameters, has received relatively little attention in current literature when compared to momentum transfer. Earliest works on heat transfer in rough-wall flows include Cope (1941) and Nunner & Hudswell (1958), which were later complemented by the extensive experimental work of Dipprey & Sabersky (1963). Miyake *et al.* (2001) investigated a sand-grain roughness model as well as spanwise-aligned two-dimensional ribs and found enhanced turbulent mixing due to large scale motions. Leonardi *et al.* (2015) investigated two-dimensional spanwise-aligned circular and square rods with varying pitch to height ratio and found the circular rods to transfer more heat at relatively less drag. More recently, Forooghi *et al.* (2018) conducted a systematic investigation of the effects of roughness effective slope, density, and height on heat transfer. They found a decrease in Stanton number for denser roughness due to sheltering effect, and established correlations between Reynolds analogy factor $(St/C_f)/(St_s/C_{fs})$ and various surface parameters. MacDonald *et al.* (2019) conducted a similar study but at a fixed roughness solidity and

increasing mean roughness height from the transitionally rough regime to the fully rough regime, where they found the temperature roughness function approaching a constant in the fully rough regime. While these works have provided some understanding on rough-wall heat transfer, systematic investigation of heat transfer over three-dimensional roughness with both varying solidity and roughness height is missing from current literature.

1.8 Rough-wall numerical simulations

Computational power has increased significantly over the last few decades, and computational fluid dynamics (CFD) is providing valuable insight into turbulence that was not always feasible with experimental methods. While there are a number of methods for fluid flow simulations, the method used in this thesis is called Direct Numerical Simulation (DNS). In DNS, the Navier–Stokes equations are directly solved on a computational grid that is sufficiently small to capture the smallest scales of turbulence, and on a domain size sufficiently large to capture the largest structures in the flow. This makes DNS quite computationally expensive as the number of degrees of freedom scales with Re_τ^3. By choosing an open channel flow in this study, the computational cost is reduced by half compared to a full channel flow. Roughness affects the flow up to the roughness sublayer, which could be in the buffer region or up into the log-layer, but not the outer layer. As the primary focus here is to investigate the effect of roughness, an open channel configuration is well-suited for this study. Also for a majority of the simulations here, the minimal-span approach is used as per the guidelines by Chung *et al.* (2015). The streamwise and spanwise domain size is decreased in minimal-span simulations, thus capturing

the flow near the wall accurately up to a critical height, z_c. The largest structures in the flow are deliberately not captured. However, by the outer-layer similarity hypothesis proposed by Townsend (1976), the outer flows can be considered to be similar. As shown by Chung *et al.* (2015); MacDonald *et al.* (2019), minimal-span simulations can accurately predict roughness functions while minimising the computational cost of higher Reynolds number flows.

1.9 Objectives

There is a clear gap in current literature that has not addressed the systematic investigation of three-dimensional roughness and its varying parameters on heat transfer. Thus, it is important to fill this gap by developing a better understanding of both the skin-friction as well as the heat transfer in rough-wall turbulent flows by taking into account a range of roughness types and geometries. This study aims to expand on the findings of current literature by investigating the effects of varying solidity of three-dimensional sinusoidal roughness on both momentum and heat transfer for a constant Prandtl number, $Pr = 0.71$. Also, the effects of varying solidity on the transitionally rough regime as well as on the roughness functions are investigated here. Chapter 1 presents the relevant background and literature, Chapter 2 presents the methodology and computational aspects of the study, Chapter 3 presents the results and discussion, and Chapter 4 presents the conclusions.

Chapter 2
Methodology

2.1 Governing equations

The governing equations introduced in Section 1.3 are numerically solved to simulate the turbulent flow through an open channel. These are given as:

$$\frac{\partial u_i}{\partial x_i} = 0 \tag{2.1}$$

$$\frac{\partial u_i}{\partial t} + \frac{\partial u_i u_j}{\partial x_j} = -\frac{1}{\rho}\frac{\partial p}{\partial x_i} + \nu\frac{\partial^2 u_i}{\partial x_j^2} + F_i\phi + f_i \tag{2.2}$$

$$\frac{\partial \theta}{\partial t} + \frac{\partial u_i \theta}{\partial x_i} = \alpha\frac{\partial^2 \theta}{\partial x_i^2} + G + f_\theta \tag{2.3}$$

where, f_i, f_θ are added force terms that originate from the immersed boundary method used in the solver to implement the roughness geometry (explained in Section 2.4).

2.2 Roughness parameters

The mathematically modeled roughness studied in this study can be defined as a sinusoidal function given by,

$$z_w = k \sin\left(\frac{2\pi x}{\lambda_x}\right) \sin\left(\frac{2\pi y}{\lambda_y}\right) + h_0 \tag{2.4}$$

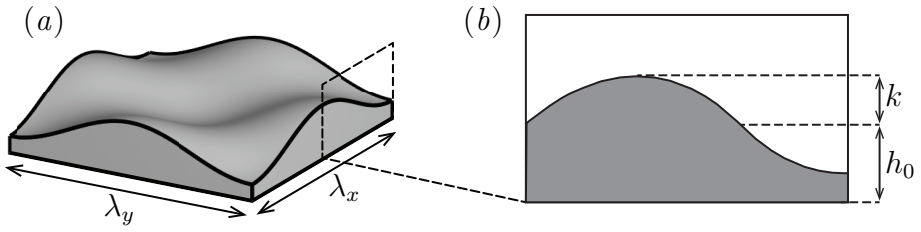

Figure 2.1: (*a*) 3-D and (*b*) 2-D sketch of unit roughness with mean roughness height, k, and wavelength, $\lambda_x = \lambda_y = \lambda$. Offset from the bottom of the domain is h_0.

where, z_w is the heightmap of the roughness measured relative to $z = 0$ (the bottom of the domain), k is the roughness height (semi-amplitude of the sine wave), $\lambda_x = \lambda_y = \lambda$ is the roughness wavelength, and h_0 is the offset of the roughness from the bottom of the computational domain. A sketch of the roughness geometry for a unit wavelength is shown in Figure 2.1. With the definition of solidity introduced earlier, it can be shown that the solidity of this roughness is $\Lambda = 4k/(\pi\lambda_x)$ (Chan *et al.*, 2015). To investigate the effect of solidity, three solidity sets are chosen: $\Lambda = 0.09$ (low), $\Lambda = 0.18$ (medium), and $\Lambda = 0.36$ (high). By repeating the unit shown in Figure 2.1, the bottom wall of the domain is constructed (Figure 2.2). 3-D sketches of the walls with three different solidities are shown in Figure 2.2, and Table 2.1 shows 2-D sketches of all of the roughness cases across all solidity sets studied.

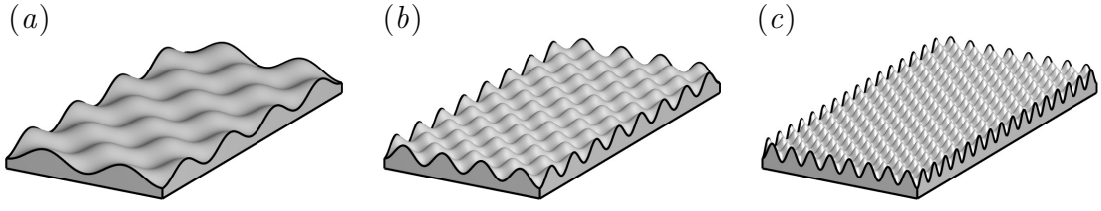

Figure 2.2: 3D sketch of (*a*) low, (*b*) medium, and (*c*) high solidity at fixed mean roughness height.

$\Lambda = 0.09$	$\Lambda = 0.18$	$\Lambda = 0.36$
 L06_079	 M11_079	 H11_039
 L11_157	 M22_157	 H22_079
 L17_235	 M33_235	 H33_117
 L20_286	 M40_286	 H40_143
 L34_477	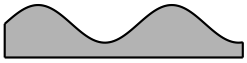 M67_477	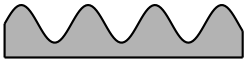 H67_239
 L40_573	 M94_668	 H94_334

Table 2.1: 2-D sketches of all roughness cases simulated in the present study. First letter of casename denotes low, medium, or high solidity, followed by roughness height, k^+, and wavelength, λ^+.

Table 2.2 lists the three solidity sets and the cases simulated for each of them. For all cases, the first letter denotes whether the case is low, medium, or high solidity, followed by the roughness height, k^+, and the wavelength, λ^+. For example, M40_286 means the case is medium solidity with a roughness height $k^+ = 40$ and wavelength $\lambda^+ = 286$. This naming convention is kept consistent with Chan *et al.* (2015) as it facilitates better comparison across multiple solidities.

For the low solidity set, the wavelength is taken to be $\lambda/k = \lambda_x/k = \lambda_y/k = 14.2$. The first case (L06_079) has a roughness height of $k/h = 0.014$, giving us $k^+ \approx 6$ at $Re_\tau = 395$. For the remaining cases, the roughness height is taken to be $k/h = 0.028$. This ensured constant blockage of the roughness, as studied by Chan *et al.* (2015). By simulating this roughness at five friction Reynolds numbers from $Re_\tau = 395$ to $Re_\tau = 1440$, five more viscous-scaled roughness heights ranging from $k^+ \approx 11$ to $k^+ \approx 40$ is obtained. In total, these six cases range from $k^+ \approx 6$ to $k^+ \approx 40$. Chan *et al.* (2015) found that $k_s/k = 4.1$ for the set of sinusoidal roughness matching the medium solidity set. Because the low solidity set is shallower, if it is estimated that $k_s/k \approx 2$, the current roughness heights are in the range of $k_s^+ \approx 12$ to $k_s^+ \approx 80$. The wavelength for the medium set is taken to be $\lambda/k = \lambda_x/k = \lambda_y/k = 7.1$, and is further reduced to $\lambda/k = \lambda_x/k = \lambda_y/k = 3.55$ for the high solidity case. For both the medium and high solidity set, the first cases (M11_079 and H11_039) have a roughness height of $k/h = 0.028$, giving us $k^+ \approx 11$ at $Re_\tau = 395$. For the remaining cases, the roughness height is taken to be $k/h = 0.056$. Because the roughness height k/h for the medium and high solidity sets is larger (Table 2.2), a similar set of friction Reynolds number gave us a larger viscous-scaled roughness, k^+. The highest k^+ case for both sets is simulated at $Re_\tau = 1680$. Thus, the cases range from $k^+ \approx 11$ to $k^+ \approx 94$. This puts us in the fully rough regime for the medium solidity as shown by MacDonald *et al.* (2019). Considering that the high solidity has a higher k_s/k, this set should be in the fully rough regime too.

2.3 Simulation setup

For the full-span simulations (L11_157 and L17_235) of the low solidity set, the domain size is set to $L_x/h \approx 2\pi$ and $L_y/h \approx \pi$ in the streamwise and spanwise direction respectively following the guidelines of Lozano-Durán & Jiménez (2014), and is adjusted to ensure an integer number of wavelengths in both directions. The number of grid points in the streamwise and spanwise direction is set in a manner to fulfill the following two conditions:

1. A minimum of $\lambda_x/\Delta_x = 24$ and $\lambda_y/\Delta_y = 48$ per wavelength (Rouhi *et al.*, 2019), and

2. $\Delta_x^+ < 10$ and $\Delta_y^+ < 5$

Although various values for Δ_x^+ and Δ_y^+ are used in literature, for example Moser *et al.* (1999) used $\Delta_x^+ < 18$ and $\Delta_y^+ < 7$, Coleman & Sandberg (2010) used $\Delta_x^+ < 15$ and $\Delta_y^+ < 8$, domain is set at a slightly higher resolution. Prandtl number imposes a limitation on grid-resolution too. In this study, the simulations were conducted at a fixed Prandtl number, $Pr = \nu/\alpha = 0.71$, which means that viscosity is smaller than thermal diffusivity. Hence, by sufficiently resolving the grid for the smallest scales of turbulence, it is ensured that the grid is well resolved for temperature as well. For the higher Re_τ cases, however, resolving the smallest turbulent scales in a full domain is computationally expensive. Hence, the domain size is reduced in both the streamwise and spanwise direction (Figure 2.3). This is the minimal-span channel approach discussed in Section 1.8. However, the domain is not 'strictly' minimal, as seen in Chung *et al.* (2015). A reduced spanwise domain size, $L_{y,m}$, only captures the flow reliably up to a critical height z_c (Figure 2.3),

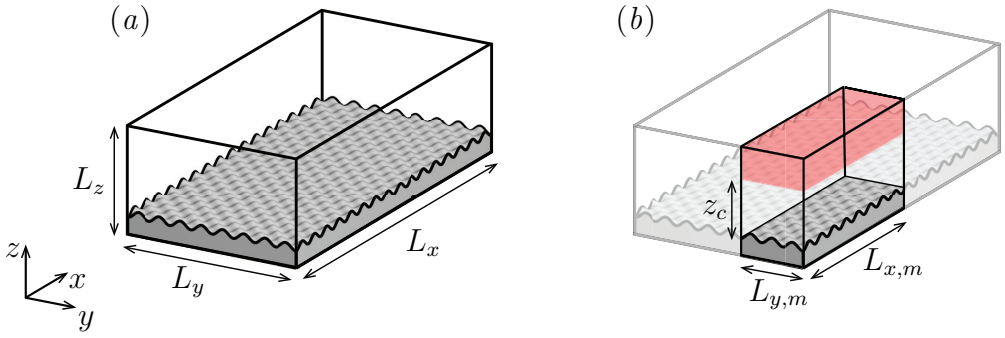

Figure 2.3: Sketch of (a) full- and (b) minimal-span channel. Minimal-span channel has shorter domain size, which makes the flow reliable up to a critical height, z_c, above which the flow is unphysical (red region).

where $z_c = 0.4L_{y,m}$. Above this critical height of a minimal-span channel, the flow is unphysical. To extend this critical height in the wall-normal direction, the spanwise domain size is kept larger than the previous studies, and ranges from $L_{y,m}/h \approx 0.99 - 1.19$. This puts the channel critical height within the range of $z_c/h \approx 0.40 - 0.48$. Here, $z_c > 0.5\lambda$ so that the channel critical height is above the roughness sublayer (Chan *et al.*, 2018). All the parameters for each case are given in Table 2.2. Domain dimensions are subsequently denoted by L_x and L_y irrespective of full- or minimal-span channel.

The spacing in wall-normal direction is kept constant, $\Delta^+_{z,b}$, from the bottom of the domain to the roughness crest for any given case, and is stretched as a tangent hyperbolic function from the crest up to the free surface, where the spacing at the cell immediately below the free surface is taken to be $\Delta^+_{z,t}$. The only constraint followed in this spacing is to have $\Delta^+_{z,b} < 1$ and $\Delta^+_{z,t} < 7$. Note that for minimal-span channel simulations, the spacing that lies above the critical height, z^+_c, is of less significance and hence is greater than the constraint for some cases, as the captured flow in that region is unphysical anyway.

For the medium solidity set, the computational domain sizing follows the same approach as the low solidity set, starting off with larger domain sizes for the lower Re_τ cases, and reducing to a smaller size for the higher Re_τ cases. Because the wavelength of the high solidity set is shorter, more wavelengths fit into the same domain size. With the minimum number of cells required per wavelength suggested by Rouhi *et al.* (2019), this becomes computationally expensive. Hence, all cases of the high solidity set were simulated in minimal-span channels. The streamwise length ranges from $L_x/h \approx 2\pi$ for the low Reynolds number cases to $L_x/h \approx \pi$ for the high Reynolds number cases. It is to be noted that for the lowest k^+ cases across all solidity sets (L06_079, M11_079, and H11_039), the roughness wavelength, λ_x has decreased due to k/h being smaller. This leads to a greater number of wavelengths in the domain and requires more grid points to fully resolve. Hence, these particular cases were simulated in a minimal-span channel despite being relatively low Reynolds number cases.

Case	Re_τ	h/k	k^+	L_x/h	L_y/h	L_x^+	L_y^+	z_c^+	N_x	N_y	N_z	Δ_x^+	Δ_y^+	$\Delta_{z,b}^+$	$\Delta_{z,t}^+$	Λ	λ_x/k	λ_x/h	λ_x/Δ_x	λ_y/Δ_y
L06_079	395	72	5.53	3.18	1.19	1256	471	188	384	288	225	3.27	1.64	0.14	8.12	0.09	14.2	0.2	48	96
L11_157	395	36	11.06	6.36	3.18	2513	1256	-	384	384	225	6.54	3.27	0.26	7.57	0.09	14.2	0.4	24	48
L17_235	590	36	16.52	6.36	3.18	3753	1877	-	512	512	300	7.33	3.67	0.38	6.19	0.09	14.2	0.4	32	64
L20_286	720	36	20.16	3.18	1.19	2290	859	344	256	192	350	8.95	4.47	0.38	6.74	0.09	14.2	0.4	32	64
L34_477	1200	36	33.60	3.18	1.19	3817	1431	573	384	288	450	9.94	4.97	0.60	7.38	0.09	14.2	0.4	48	96
L40_573	1440	36	40.32	3.18	1.19	4580	1718	687	496	360	450	9.23	4.77	0.76	8.42	0.09	14.2	0.4	62	120
M11_079	395	36	11.06	3.18	1.19	1256	471	188	384	288	225	3.27	1.64	0.26	7.40	0.18	7.1	0.2	48	96
M22_157	395	18	22.12	6.36	3.18	2513	1256	-	384	384	225	6.54	3.27	0.51	6.05	0.18	7.1	0.4	24	48
M33_235	590	18	33.04	6.36	3.18	3753	1877	-	512	512	300	7.33	3.67	0.76	4.82	0.18	7.1	0.4	32	64
M40_286	720	18	40.32	3.18	1.19	2290	859	344	256	192	350	8.95	4.47	0.60	7.05	0.18	7.1	0.4	32	64
M67_477	1200	18	67.20	3.18	1.19	3817	1431	573	384	288	500	9.94	4.97	0.75	7.49	0.18	7.1	0.4	48	96
M94_668	1680	18	94.08	3.18	1.19	5344	2004	802	544	408	650	9.82	4.91	0.77	8.61	0.18	7.1	0.4	68	136
H11_039	395	36	11.06	3.18	0.99	1256	393	157	768	480	225	1.64	0.82	0.26	7.40	0.36	3.55	0.1	48	96
H22_079	395	18	22.12	6.36	0.99	2513	393	157	768	240	225	3.27	1.64	0.51	6.05	0.36	3.55	0.2	24	48
H33_117	590	18	33.04	6.36	0.99	3753	586	235	768	240	300	4.89	2.44	0.76	4.82	0.36	3.55	0.2	24	48
H40_143	720	18	40.32	3.18	0.99	2290	716	286	384	240	300	5.96	2.98	0.76	5.27	0.36	3.55	0.2	24	48
H67_239	1200	18	67.20	3.18	0.99	3817	1193	477	384	240	500	9.94	4.97	0.77	7.27	0.36	3.55	0.2	24	48
H94_334	1680	18	94.08	3.18	0.99	5344	1670	668	544	340	650	9.82	4.91	0.77	8.61	0.36	3.55	0.2	34	68

Table 2.2: Description of the different cases simulated. h/k is the blockage ratio, $\Delta_{z,b}^+$ is the constant wall-normal grid spacing from the bottom of the domain to the roughness crest, and $\Delta_{z,t}^+$ is the grid spacing at the cell immediately below the free surface. Cases L11_157, L17_235, M22_157, and M33_235 are full-span while the rest are minimal-span simulations. All cases are simulated at a constant Prandtl number, $Pr = 0.71$, and CFL = 0.25.

2.4 Numerical methods and solver

The code used in this study was used in previous DNS studies (Chung *et al.*, 2014, 2015; Rouhi *et al.*, 2019). The governing equations are spatially discretised using the fully conservative fourth-order staggered finite-difference scheme formulated by Verstappen & Veldman (2003), and is marched forward in time using the low-storage third-order Runge-Kutta scheme of Wray given by Spalart *et al.* (1991). This scheme contains a second-order implicit treatment, which is used for the wall-normal viscous term. The equations are integrated using the fractional step method (Perot, 1993).

The no-slip boundary condition along the roughness geometry on the bottom surface is imposed through a 'direct-forcing' immersed boundary method (IBM) based on the volume of fluid (VOF) approach (Fadlun *et al.*, 2000). The force fields f_i and f_θ in (2.2) and (2.3) are interpolated based on the VOF in each computational cell of the domain. This approach has been used in previous DNS studies such as Scotti (2006) and Yuan & Piomelli (2014). In the pre-processing stage, each computational cell is divided into a number of subcells. The VOF in such a computational cell is determined as a fraction, based on the number of subcells lying in either the solid or the fluid region, and the whole cell is assigned a value from 0 to 1, where 0 represents the cell is completely in the solid region and 1 represents the cell is completely in the fluid region (Figure 2.4). To ensure that $f_i = 0$ in the solid region, the mean pressure gradient, F_i is multiplied by ϕ_i since there is no pressure gradient in the solid region (Rouhi *et al.*, 2019).

The wall shear stress as well as the heat flux can be calculated using this approach. As established in Section 1.4, by integrating the governing equations, the

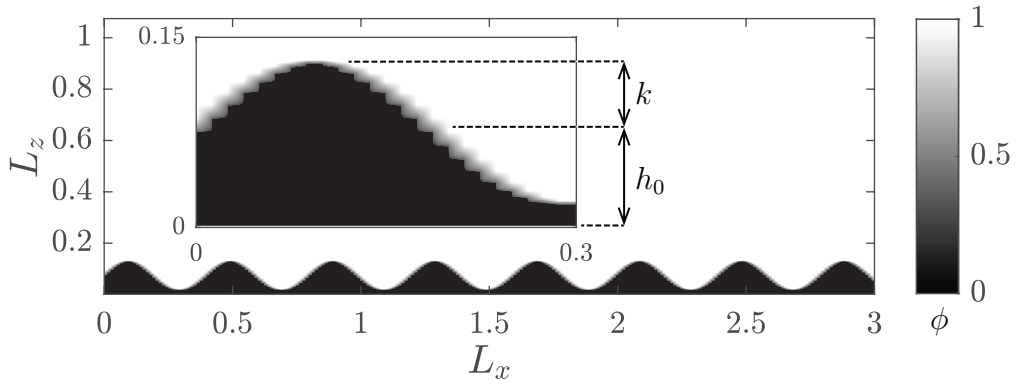

Figure 2.4: Visualisation of roughness with the volume of fluid, ϕ. Inset shows the implementation of roughness geometry, where $\phi = 0$ in the solid region and $\phi = 1$ in the fluid region. The mean roughness height is k, and the rough-wall is offset from the bottom of the computational domain by a distance h_0, such that $L_z = h + h_0$.

following two relations can be found:

$$\frac{\tau_w}{\rho} \equiv -\frac{h}{\rho}\frac{\mathrm{d}P}{\mathrm{d}x} \tag{2.5}$$

$$U_b\frac{\mathrm{d}T}{\mathrm{d}x} \equiv -\frac{q_w}{h\rho c_p} \tag{2.6}$$

Now, when the immersed boundary method is used, (2.2) and (2.3) can be integrated to establish,

$$-\langle f_1\rangle = \langle F_1\phi\rangle = -\frac{1}{\rho}\frac{\mathrm{d}P}{\mathrm{d}x}\langle\phi\rangle \tag{2.7}$$

$$-\langle f_\theta\rangle = \langle G\rangle = -\langle u\rangle\frac{\mathrm{d}T}{\mathrm{d}x} \tag{2.8}$$

where, $\langle\cdot\rangle$ means the term is averaged in the $x-y$ direction and integrated in $z-$direction. Comparing $(2.5-2.8)$, it is obtained,

$$-\langle f_1 \rangle \equiv \frac{\tau_w}{\rho} \tag{2.9}$$

$$-\langle f_\theta \rangle \equiv \frac{q_w}{\rho c_p} \tag{2.10}$$

The body forces for both the momentum and temperature can thus be used to calculate the wall shear stress and the heat flux respectively. Due to the nature of the immersed boundary method, the wall shear stress includes both the viscous drag and the form (pressure) drag (Rouhi *et al.*, 2019). Note that the flow is considered incompressible in this study and there is no variation in density. The computational solver already normalises by density as it is an incompressible solver, so the immersed boundary force is normalised by density by definition.

In the solver, L_z is specified as an input along with the domain dimensions L_x and L_y, viscosity ν, timestep size or a constant Courant-Friedrichs-Lewy (CFL) number, Prandtl number Pr, the mean pressure gradient $(1/\rho)\mathrm{d}P/\mathrm{d}x$, and the mean temperature gradient $\mathrm{d}T/\mathrm{d}x$. With a specified domain height $h = 1$, and a mean pressure gradient $(1/\rho)\mathrm{d}P/\mathrm{d}x = -1$, it is obtained $\tau_w/\rho = -(h/\rho)\mathrm{d}P/\mathrm{d}x = 1$. Thus, $u_\tau = \sqrt{\tau_w/\rho} = 1$. Similarly, the friction temperature is taken to be $\theta_\tau = q_w/(u_\tau \rho c_p)$. From (2.10) and (2.8), it can be seen that by setting $\mathrm{d}T/\mathrm{d}x = 1$, it can obtained $\theta_\tau = -U_b^+$, where $U_b^+ = U_b/u_\tau$. Because $Re_\tau = hu_\tau/\nu$ where both h and u_τ are unity, a target global friction Reynolds number can be reached only by specifying $\nu = 1/Re_\tau$. To initiate a simulation, five input files are required: VOF files `u`, `v`, `w`, `p`, and the wall-normal grid file, `dz`. A separate VOF file is not required for the temperature as it uses the same VOF file, `p`, as that of pressure. Table 2.3 shows a summary of all simulations conducted in this study. Because the simulations are conducted at a constant CFL, instantaneous timestep sizes are

different. The non-dimensionalised average timestep sizes, $\Delta t_{avg} = \Delta t u_\tau / h$ (for full-span channels) and $\Delta t_{avg} = \Delta t u_\tau / z_c$ (for minimal-span channels), are shown in the table. $T_{avg} = T u_\tau / h$ (for full-span channels) and $T_{avg} = T u_\tau / z_c$ (for minimal-span channels) are the simulation times for which the time-averaging is performed. For all cases, statistics are collected after transients are discarded. Full-span channels are averaged over a minimum window of $T_{avg} > 5$ and minimal-span channels are averaged over a minimum window of $T_{avg} > 10$, although most cases are greater than this minimum value.

Case	Re_τ	h/k	k^+	Λ	$N_x \times N_y \times N_z$	Δt_{avg}	T_{avg}
L06_079	395	72	5.53	0.09	$384 \times 288 \times 225$	4.58×10^{-5}	25.68
L11_157	395	36	11.06	0.09	$384 \times 384 \times 225$	4.16×10^{-5}	12.48
L17_235	590	36	16.52	0.09	$512 \times 512 \times 300$	3.09×10^{-5}	6.26
L20_286	720	36	20.16	0.09	$256 \times 192 \times 350$	2.53×10^{-5}	19.27
L34_477	1200	36	33.60	0.09	$384 \times 288 \times 450$	1.74×10^{-5}	12.28
L40_573	1440	36	40.32	0.09	$496 \times 360 \times 450$	1.73×10^{-5}	11.84
M11_079	395	36	11.06	0.18	$384 \times 288 \times 225$	5.05×10^{-5}	12.01
M22_157	395	18	22.12	0.18	$384 \times 384 \times 225$	6.52×10^{-5}	14.07
M33_235	590	18	33.04	0.18	$512 \times 512 \times 300$	5.23×10^{-5}	10.67
M40_286	720	18	40.32	0.18	$256 \times 192 \times 350$	3.72×10^{-5}	24.06
M67_477	1200	18	67.20	0.18	$384 \times 288 \times 500$	2.08×10^{-5}	11.47
M94_668	1680	18	94.08	0.18	$544 \times 408 \times 650$	1.42×10^{-5}	10.48
H11_039	395	36	11.06	0.36	$768 \times 480 \times 225$	5.05×10^{-5}	11.80
H22_079	395	18	22.12	0.36	$768 \times 240 \times 225$	8.21×10^{-5}	38.52
H33_117	590	18	33.04	0.36	$768 \times 240 \times 300$	6.84×10^{-5}	38.20
H40_143	720	18	40.32	0.36	$384 \times 240 \times 350$	5.29×10^{-5}	19.59
H67_239	1200	18	67.20	0.36	$384 \times 240 \times 500$	2.91×10^{-5}	12.35
H94_334	1680	18	94.08	0.36	$544 \times 340 \times 650$	1.77×10^{-5}	13.37

Table 2.3: Summary of simulations with average timestep size, Δt_{avg}, and simulation time of time-averaging, T_{avg}. Cases L11_157, L17_235, M22_157, and M33_235 are full-span while the rest are minimal-span simulations. All cases are simulated at CFL = 0.25.

2.5 Validation

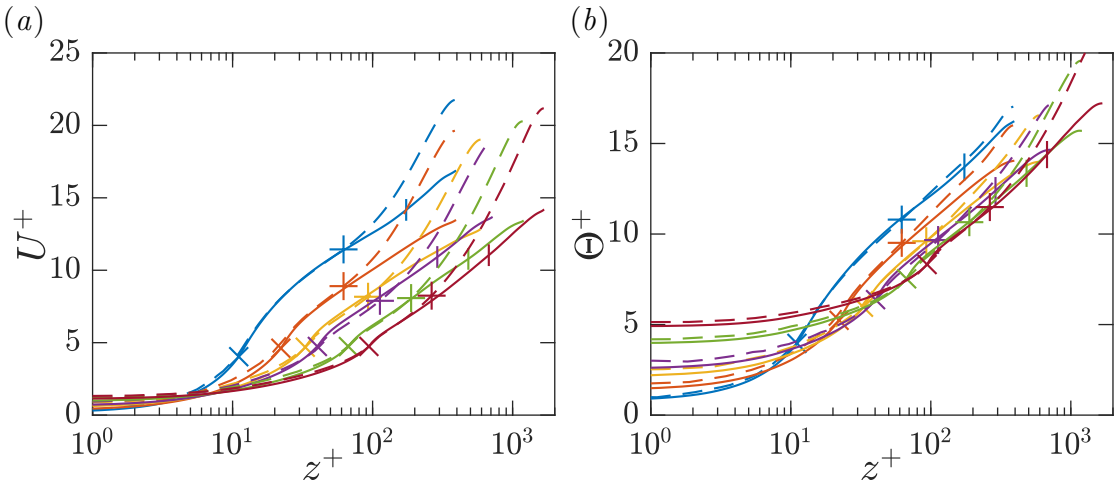

Figure 2.5: (a) Mean velocity and (b) mean temperature profiles for medium solidity open channels (solid lines) with increasing roughness height. Dashed lines denote MacDonald *et al.* (2019) data. Colours and symbols: (—) $k^+ \approx 11$, $Re_\tau = 395$; (—) $k^+ \approx 22$, $Re_\tau = 395$; (—) $k^+ \approx 33$, $Re_\tau = 590$; (—) $k^+ \approx 40$, $Re_\tau = 720$; (—) $k^+ \approx 67$, $Re_\tau = 1200$; (—) $k^+ \approx 94$, $Re_\tau = 1680$; ($\times$) roughness crest; (|) critical channel height of current study, z_c^+; (+) critical channel height of MacDonald *et al.* (2019), $z_{c,M}^+$.

The accuracy of the solver is verified by comparing the velocity and temperature profiles of the medium solidity set, $\Lambda = 0.18$ to those of MacDonald *et al.* (2019). For all cases, intrinsic averaging is used. Because MacDonald *et al.* (2019) used a body-fitted grid and this study utilised an immersed-boundary method with VOF approach (Rouhi *et al.*, 2019), some difference is seen below the roughness crest, yet the velocity profiles in Figure 2.5(a) are in good agreement above the roughness crest. The temperature profiles in Figure 2.5(b) also show overall good agreement with slight disagreement below the roughness crest due to the different grids used across these studies. Some discrepancies between the current study and MacDonald *et al.* (2019) can be seen in the region $k^+ \lesssim z^+ \lesssim z_{c,M}^+$, where $z_{c,M}^+$ is the channel critical height of MacDonald *et al.* (2019). In this region, the current study slightly

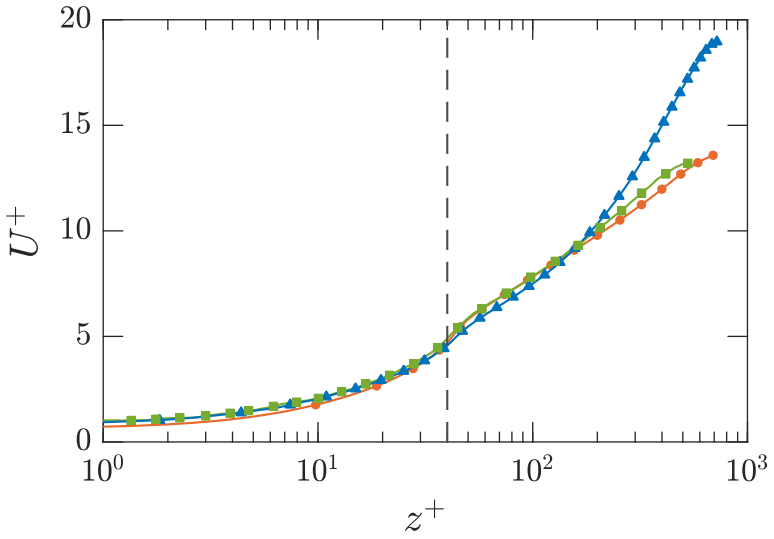

Figure 2.6: Mean velocity profile for current rough-wall open channel data and existing literature. Symbols: (●) M40_286 ; (▲) (MacDonald *et al.*, 2019); (■) (Chan *et al.*, 2015). Vertical dashed-line marks the roughness crest.

overestimates the mean velocity profile. As Chan *et al.* (2015) performed a similar set of simulations for pipe flow at $\Lambda = 0.18$, a matching case of $k^+ \approx 40$ was compared to both the current study and MacDonald *et al.* (2019) case. Figure 2.6 shows that the current study has better agreement to Chan *et al.* (2015), who also show a slight overestimation in the same region. This may be due to the fact that the roughness sublayer, characterised by coherent fluctuations which can extend in the wall-normal direction, is a function of the spanwise wavelength and can extend up to $z^+ \approx 0.5\lambda^+$ (Chan *et al.*, 2018). Because MacDonald *et al.* (2019) conducted their simulation in 'strictly' minimal-span channels, their channel critical height $z^+_{c,M}$ lies below $0.5\lambda^+$. Hence, their time-averaged velocity field slightly differs from the current study as well as Chan *et al.* (2015).

The velocity and temperature roughness functions (ΔU^+ and $\Delta\Theta^+$) for the medium solidity cases are also compared to MacDonald *et al.* (2019) (Figure 2.7).

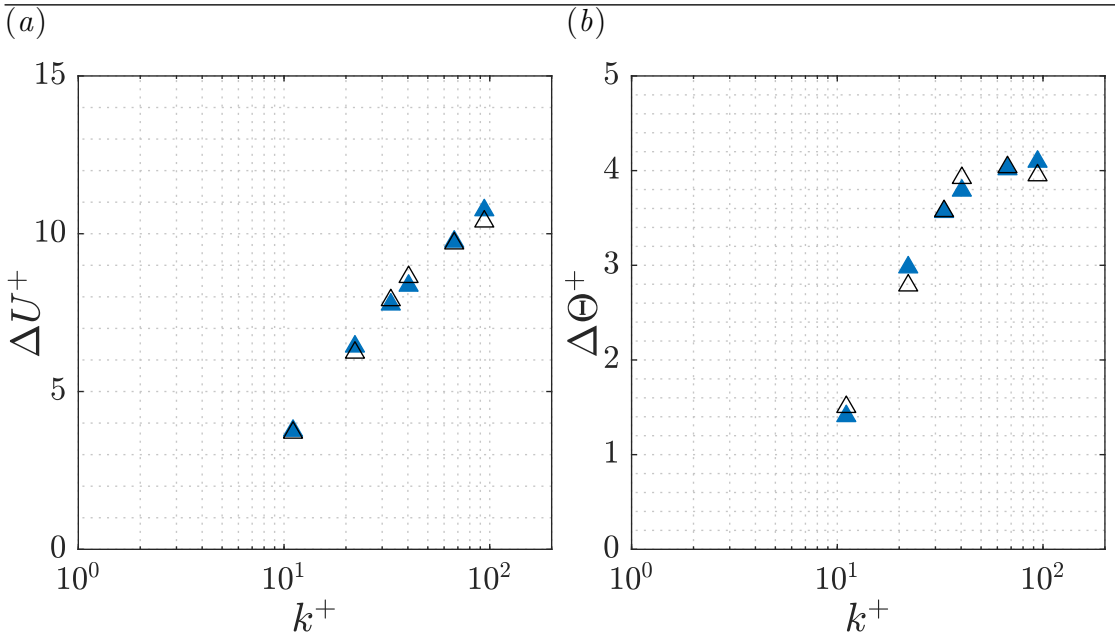

Figure 2.7: (a) Momentum and (b) temperature roughness functions for medium solidity. Symbols: △, MacDonald *et al.* (2019); ▲, present (medium solidity, $\Lambda = 0.18$).

For minimal-span channel simulations, the dimensions of the domain affect the critical channel height, $z_c = 0.4L_y$. Because the minimal-span channel simulations in this study use a wider span compared to MacDonald *et al.* (2019), the corresponding critical heights are also higher. To ensure a fair comparison, the roughness functions for the current medium solidity cases were calculated at matching heights, $z^+_{c,M}$, where MacDonald *et al.* (2019) calculated their roughness functions. In this section, $\Delta U^+ = U^+_s(z^+_{c,M}) - U^+_r(z^+_{c,M})$ and $\Delta\Theta^+ = \Theta^+_s(z^+_{c,M}) - \Theta^+_r(z^+_{c,M})$. Here, $U^+_s(z^+_{c,M})$ and $\Theta^+_s(z^+_{c,M})$ are smooth-wall data taken from Bernardini *et al.* (2014) and Pirozzoli *et al.* (2016) respectively, and $U^+_r(z^+_{c,M})$ and $\Theta^+_r(z^+_{c,M})$ are rough-wall data from present study. MacDonald *et al.* (2019) reported their roughness functions based on their corresponding smooth-wall simulations. Their roughness functions (ΔU^+_M and $\Delta\Theta^+_M$) were recalculated using the reference smooth-wall pro-

files of Bernardini *et al.* (2014); Pirozzoli *et al.* (2016) to ensure better comparison, such that $\Delta U_M^+ = U_s^+(z_{c,M}^+) - U_{r,M}^+(z_{c,M}^+)$ and $\Delta\Theta_M^+ = \Theta_s^+(z_{c,M}^+) - \Theta_{r,M}^+(z_{c,M}^+)$, where $U_{r,M}^+(z_{c,M}^+)$ and $\Theta_{r,M}^+(z_{c,M}^+)$ are the velocity and temperature profile of MacDonald *et al.* (2019) respectively. This shows good agreement (Figure 2.7) between the present study and MacDonald *et al.* (2019), thus validating the data acquired in the present study.

Chapter 3
Results

3.1 Mean statistics

The three-dimensional, time-dependent streamwise velocity $u(x, y, z, t)$ and temperature $\theta(x, y, z, t)$ for all cases are averaged in $x - y$ direction and in time, t. These quantities now depend only on the wall-normal direction, z. Normalising the velocity with the friction velocity u_τ and temperature with the friction temperature θ_τ as introduced in Section 1.5, the velocity and the temperature profile is obtained as U^+ and Θ^+ respectively. Similarly, the wall-normal location z is normalised using both the friction velocity u_τ and the viscosity ν, giving $z^+ = zu_\tau/\nu$. All cases are intrinsically averaged.

The profiles are plotted on a logarithmic scale to better distinguish the multiple regions of a turbulent velocity/temperature profile as discussed previously. The velocity profiles in Figure 3.1(a), 3.2(a), and 3.3(a) show that the velocity at the wall ($z^+ = 0$) is approaching zero because of the no-slip boundary condition imposed at the wall. Moving up from the wall, the velocity first increases in a linear fashion, consistent with the viscous sublayer velocity profile (1.20), the region where viscous effects are dominant. However, the velocity profile increases logarithmically with wall height, confirming the existence of the log-layer (von Kármán, 1930). This is true for all velocity profiles, regardless of smooth- (black solid line) or rough-wall, due to the outer-layer similarity hypothesis of Townsend (1976). The tempera-

ture profiles also show similar behaviour in Figure 3.1(b), 3.2(b), and 3.3(b). The temperature at the wall ($z^+ = 0$) can be seen approaching the prescribed wall temperature ($\Theta_w^+ = 0$). Moving up from the wall, the linear behaviour characterised by (1.28) can be observed, and a similar logarithmic region to that of the velocity profile can be seen further up from the wall for both smooth- (black solid line) and rough-wall temperature profiles.

With increasing roughness height, k^+, each velocity profile in Figure 3.1(a), 3.2(a), and 3.3(a) shows the well documented downward shift, where the rough-wall velocity profile shifts parallely downwards from that of a smooth wall by an amount $\Delta U^+ = U_s^+ - U_r^+$, where U_s^+ and U_r^+ is the smooth- and rough-wall velocity profile respectively. The insets of the same figures show this difference, signifying the increase in roughness function, ΔU^+.

Figure 3.1(c), 3.2(c), and 3.3(c) also show that the velocity profiles, when plotted against z/k, are gradually collapsing for increasing k^+, indicating the onset of the fully-rough state. This can also be visualised from the insets of the same figures, where it can be noticed that the momentum at the roughness crest is approaching a constant value. For the low solidity set ($\Lambda = 0.09$), the inset of Figure 3.1(c) shows a small increasing tendency, signifying that the fully rough regime is not completely reached. However, for the medium and high solidity sets, insets of Figure 3.2(c) and 3.3(c) show the momentum has reached a constant value, signifying that the fully rough regime is reached.

The mean temperature profiles in Figure 3.1(b), 3.2(b), and 3.3(b) show a similar downward shift to that of the momentum. Here, the profiles slowly start to collapse as well, and it can be concluded that $\Delta\Theta^+ = \Theta_s^+ - \Theta_r^+$ will reach a constant value with sufficiently high k^+ and will become independent of roughness height. The

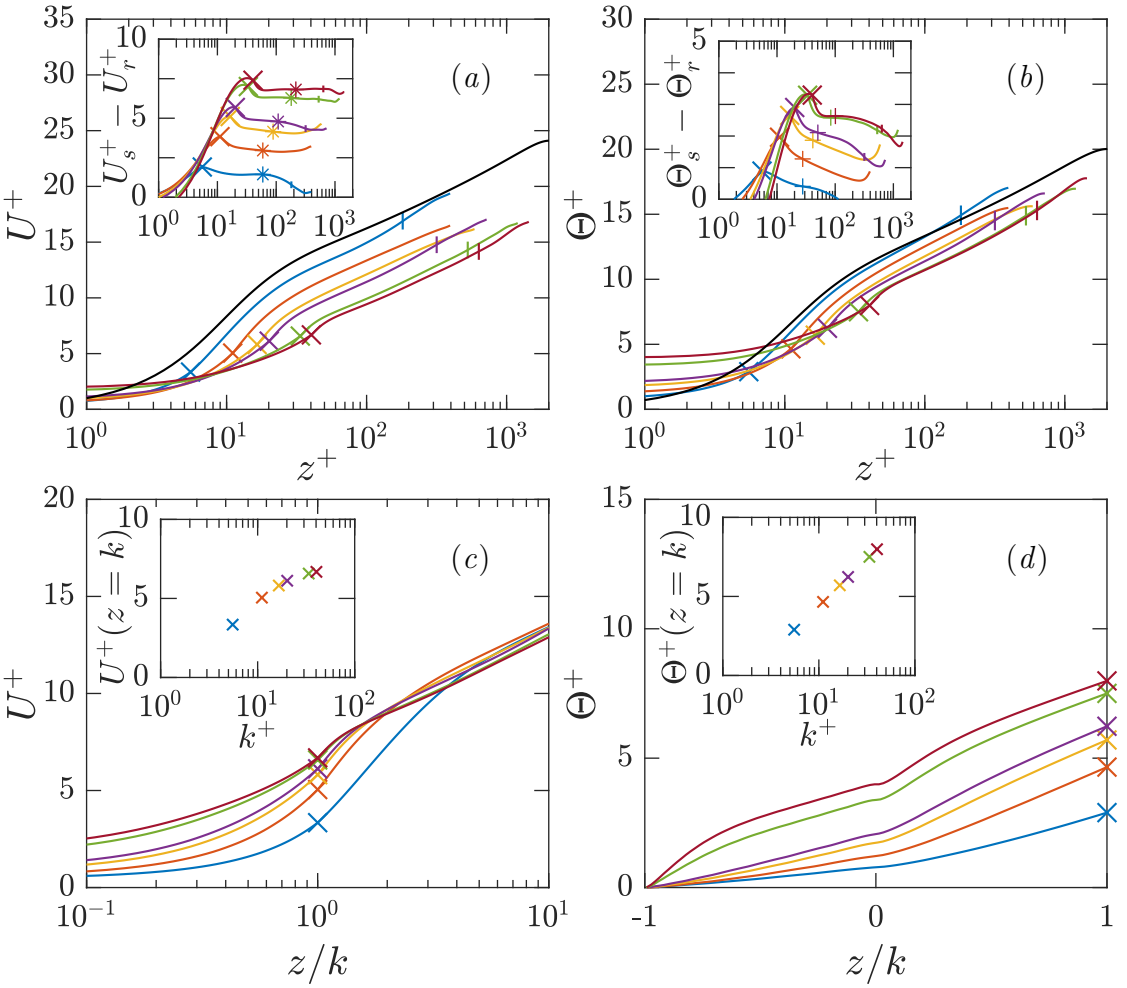

Figure 3.1: (a) Mean velocity and (b) mean temperature profiles for rough-wall open channels for low solidity, $\Lambda = 0.09$. Roughness Reynolds number increases from top to bottom. Black solid lines are the reference smooth-wall profiles from (a) Bernardini *et al.* (2014), and (b) Pirozzoli *et al.* (2016). Insets show the roughness functions ($U_s^+ - U_r^+$, $\Theta_s^+ - \Theta_r^+$) against wall-normal location, z^+, where (U_s^+, Θ_s^+) are the reference smooth-wall profiles and (U_r^+, Θ_r^+) are the current rough-wall profiles. Rough-wall (c) velocity and (d) temperature profiles against z/k. Roughness crest velocity and temperature is plotted against k^+ in the insets of (c) and (d) respectively. Colours and symbols: (—) L06_079; (—) L11_157; (—) L17_235; (—) L20_286; (—) L34_477; (—) L40_573; ($\times$) roughness crest; (|) critical channel height, z_c^+; ($*$) calculation height of ΔU^+, $z = 0.15h + d$; (+) calculation height of $\Delta\Theta^+$, $z = 0.07h + d$.

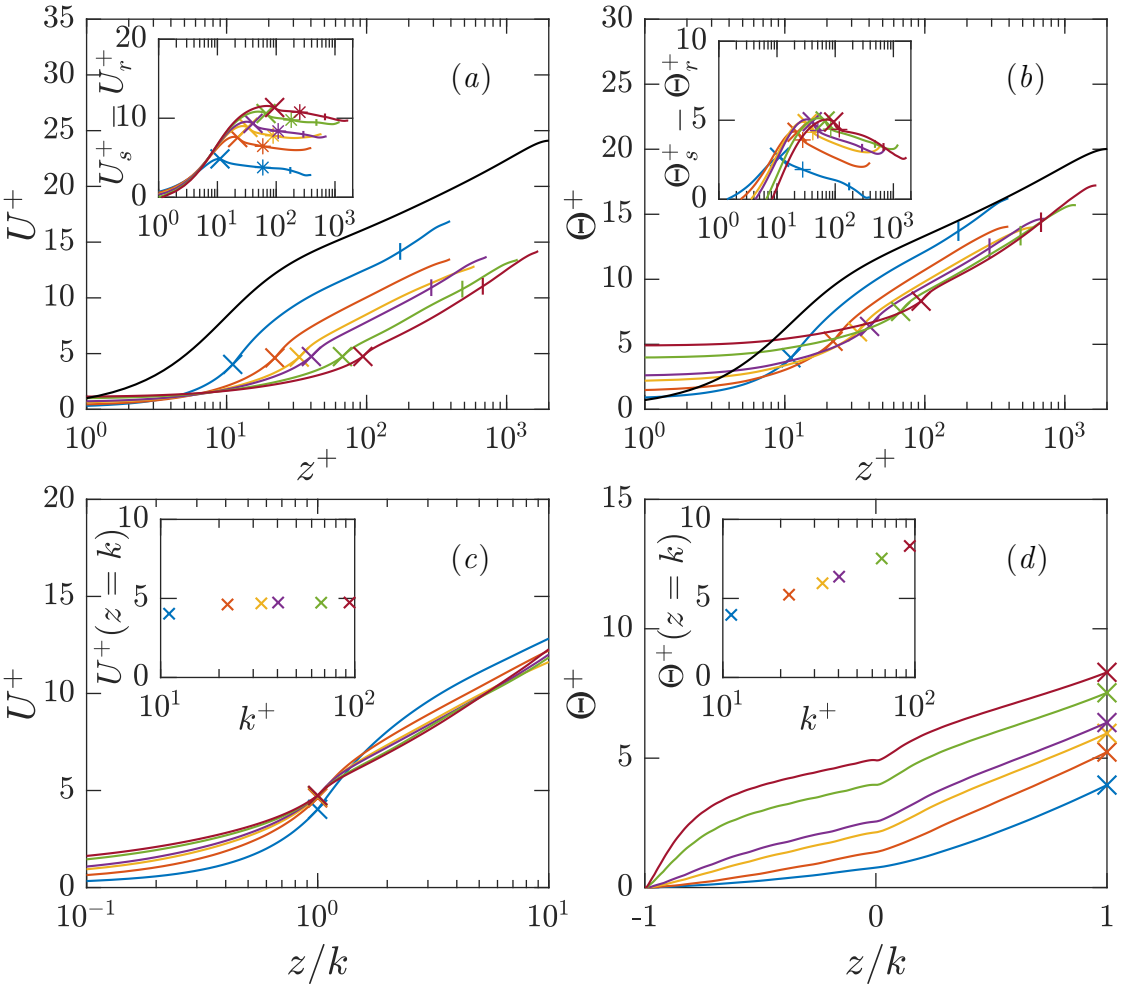

Figure 3.2: (a) Mean velocity and (b) mean temperature profiles for rough-wall open channels for medium solidity, $\Lambda = 0.18$. Roughness Reynolds number increases from top to bottom. Black solid lines are the reference smooth-wall profiles from (a) Bernardini *et al.* (2014), and (b) Pirozzoli *et al.* (2016). Insets show the roughness functions ($U_s^+ - U_r^+$, $\Theta_s^+ - \Theta_r^+$) against wall-normal location, z^+, where (U_s^+, Θ_s^+) are the reference smooth-wall profiles and (U_r^+, Θ_r^+) are the current rough-wall profiles. Rough-wall (c) velocity and (d) temperature profiles against z/k. Roughness crest velocity and temperature is plotted against k^+ in the insets of (c) and (d) respectively. Colours and symbols: (—) M11_079; (—) M22_157; (—) M33_235; (—) M40_286; (—) M67_477; (—) M94_668; (×) roughness crest; (|) critical channel height, z_c^+; (∗) calculation height of ΔU^+, $z = 0.15h + d$; (+) calculation height of $\Delta\Theta^+$, $z = 0.07h + d$.

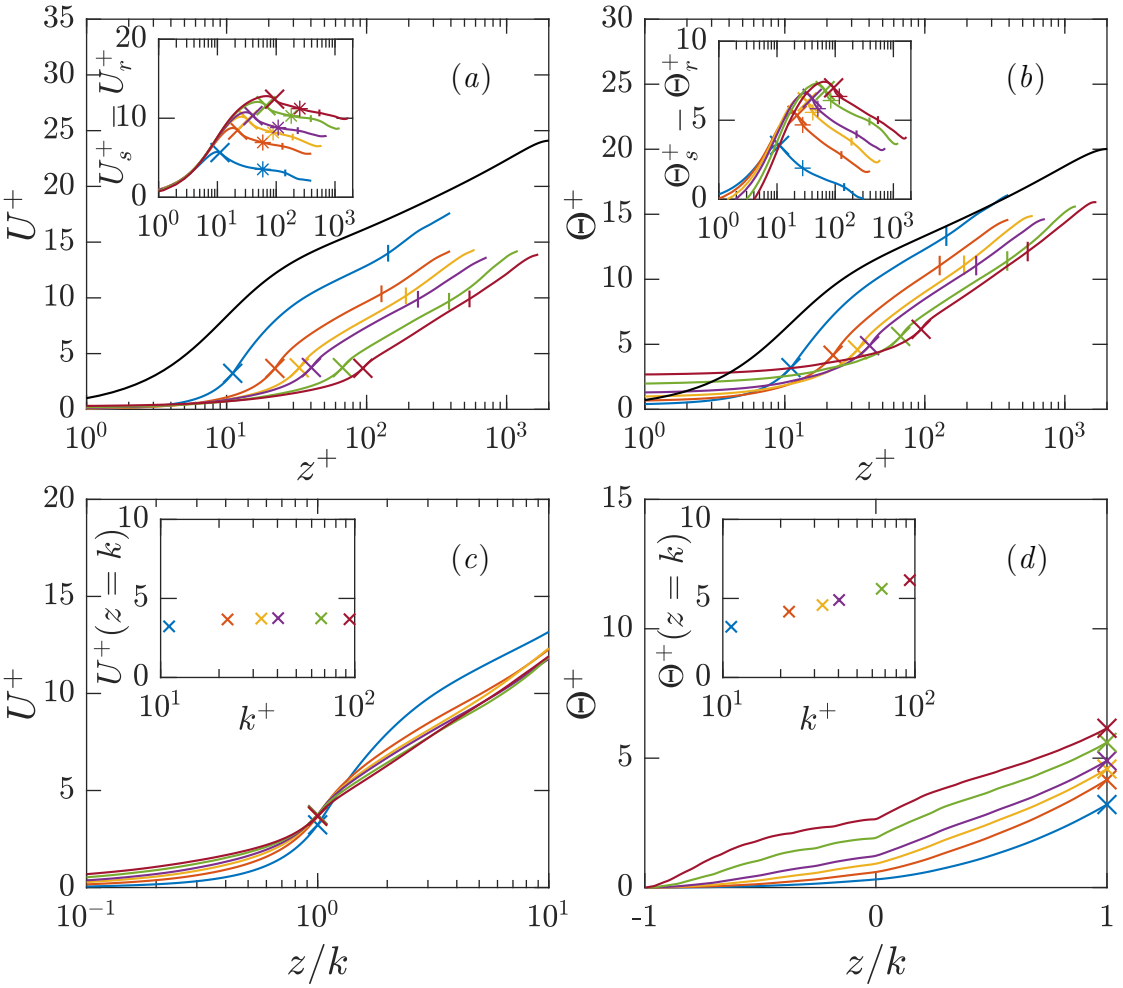

Figure 3.3: (a) Mean velocity and (b) mean temperature profiles for rough-wall open channels for high solidity, $\Lambda = 0.36$. Roughness Reynolds number increases from top to bottom. Black solid lines are the reference smooth-wall profiles from (a) Bernardini *et al.* (2014), and (b) Pirozzoli *et al.* (2016). Insets show the roughness functions ($U_s^+ - U_r^+$, $\Theta_s^+ - \Theta_r^+$) against wall-normal location, z^+, where (U_s^+, Θ_s^+) are the reference smooth-wall profiles and (U_r^+, Θ_r^+) are the current rough-wall profiles. Rough-wall (c) velocity and (d) temperature profiles against z/k. Roughness crest velocity and temperature is plotted against k^+ in the insets of (c) and (d) respectively. Colours and symbols: (—) H11_039; (—) H22_079; (—) H33_117; (—) H40_143; (—) H67_239; (—) H94_334; ($\times$) roughness crest; (|) critical channel height, z_c^+; ($*$) calculation height of ΔU^+, $z = 0.15h + d$; ($+$) calculation height of $\Delta\Theta^+$, $z = 0.07h + d$.

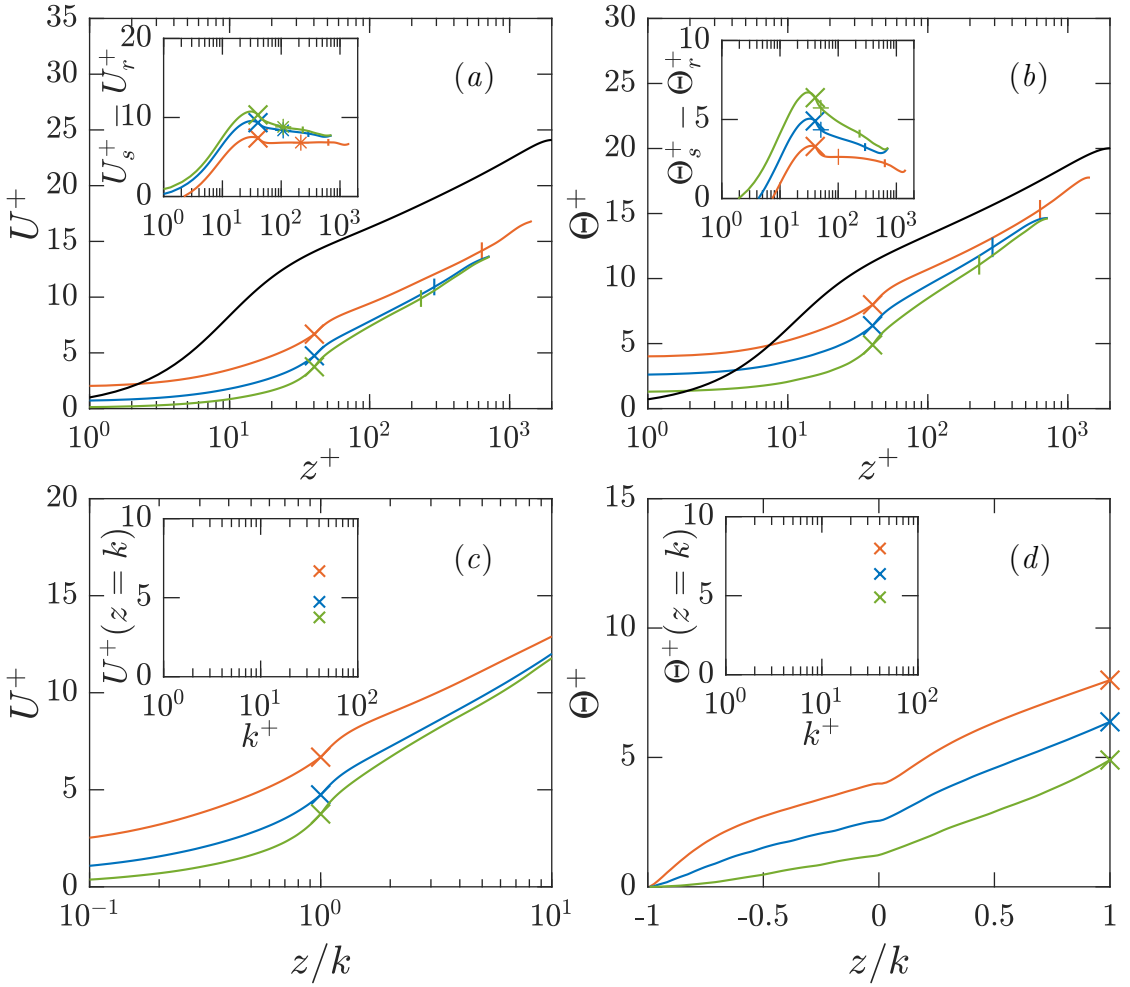

Figure 3.4: (a) Mean velocity and (b) mean temperature profiles for rough-wall open channels for all solidity sets at fixed roughness height, $k^+ = 40$. Black solid lines are the reference smooth-wall profiles from (a) Bernardini *et al.* (2014), and (b) Pirozzoli *et al.* (2016). Insets show the roughness functions ($U_s^+ - U_r^+$, $\Theta_s^+ - \Theta_r^+$) against wall-normal location, z^+, where (U_s^+, Θ_s^+) are the reference smooth-wall profiles and (U_r^+, Θ_r^+) are the current rough-wall profiles. Rough-wall (c) velocity and (d) temperature profiles against z/k. Roughness crest velocity and temperature is plotted against k^+ in the insets of (c) and (d) respectively. Colours and symbols: (—) L40_573; (—) M40_286; (—) H40_143; ($\times$) roughness crest; (|) critical channel height, z_c^+; ($*$) calculation height of ΔU^+, $z = 0.15h + d$; ($+$) calculation height of $\Delta\Theta^+$, $z = 0.07h + d$.

temperature below the roughness crest also increases with increasing roughness height. It is to be noted that for each case across all solidity sets, the $\Theta_s^+ - \Theta_r^+$ plots in the inset of Figure 3.1(b), 3.2(b), and 3.3(b) show a consistent drop because of the difference between the slope of the logarithmic region of the reference temperature profile and that of the present studies. For turbulent flow, (1.17) gives,

$$0 = -\frac{\mathrm{d}\overline{\theta' w'}}{\mathrm{d}z} + \alpha \frac{\mathrm{d}^2\Theta}{\mathrm{d}z^2} + G$$

where, $G = -U\frac{\mathrm{d}T}{\mathrm{d}x}$ is different for every rough-wall case owing to the difference in U. Thus, the slope of the logarithmic region for the temperature profile of every case is slightly different unlike the velocity profiles.

Figure 3.4 shows the profiles for all solidity sets for a fixed roughness height, $k^+ = 40$. A preliminary look at the effect of solidity shows that increasing solidity increases both velocity and temperature roughness functions (insets of Figure 3.4(a, b). However, this effect is less prominent for medium to high solidity than it is for low to medium solidity. This can be explained due the surface roughness becoming 'denser' with increasing solidity and slowly reaching an asymptotic value, and for $\Lambda \to \infty$, the surface can be expected to behave almost like a smooth wall (MacDonald *et al.*, 2016). A difference for increasing solidity can be seen in the slope of the velocity profiles in the logarithmic region. It seems that for high solidity cases, the slope becomes steeper when compared to low solidity cases (inset of Figure 3.4(a)). This introduces a consistent drop in the $U_s^+ - U_r^+$ plots, hence proving it difficult to calculate the roughness functions. This will be addressed in the following section.

3.2 Investigation of virtual origin

For the high solidity set, estimating the roughness function can prove to be difficult, as there is a consistent drop in $U_s^+ - U_r^+$ (inset of Figure 3.3(a)) originating from what seems to be a difference in the slope of the log-layer. This difference can be attributed to the shift in virtual origin, as with densely-packed roughness, the flow perceives the wall to be at a higher location compared to the mean roughness height taken as the origin. To compute this shift in the virtual origin, Chan *et al.* (2015) investigated a number of methods. In this study, the suggestions by Luchini *et al.* (1991) were followed. They suggest that the origin of turbulence is displaced upward in rough-wall flows, which can be seen as a shift in the turbulent component of the Reynolds shear stress $\overline{u'w'}^+$ compared to that of a smooth-wall under the same conditions.

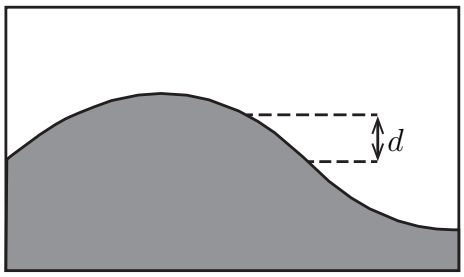

Figure 3.5: Virtual origin shift, d, where $d = 0$ locates the average height of the sinusoids.

Based on the suggestions of Luchini *et al.* (1991), the virtual origin was calculated by shifting the Reynolds stress profile of each case in a manner such that it collapses on to the Reynolds stress profile of a smooth-wall case near the wall. The reference smooth-wall cases at matched or similar friction Reynolds numbers are taken from Abe *et al.* (2001, 2004); Kozuka *et al.* (2009). This shift in the virtual

Case	Re_τ	k^+	d^+	d/k
L06_079	395	5.53	−1.1	−0.22
L11_157	395	11.06	0	0
L17_235	590	16.52	1.2	0.07
L20_286	720	20.16	2.4	0.12
L34_477	1200	33.60	4.2	0.13
L40_573	1440	40.32	4.8	0.12
M11_079	395	11.06	0.5	0.05
M22_157	395	22.12	4.1	0.19
M33_235	590	33.04	7.8	0.24
M40_286	720	40.32	11.2	0.28
M67_477	1200	67.20	24.0	0.36
M94_668	1680	94.08	32.3	0.34
H11_039	395	11.06	2.1	0.19
H22_079	395	22.12	5.6	0.25
H33_117	590	33.04	11.0	0.33
H40_143	720	40.32	16.5	0.41
H67_239	1200	67.20	33.5	0.50
H94_334	1680	94.08	47.0	0.50

Table 3.1: Virtual origin shift, d^+, for all rough-wall cases. Ratio of virtual origin shift to mean roughness height is denoted by d/k. $d = 0$ locates the average height of the sinusoids. A negative value means that the virtual origin has shifted downwards from the average height (Figure 3.5).

origin is taken as d from the mean roughness height k (Figure 3.5). Table 3.1 lists the shift in virtual origin for all cases.

In Figure 3.6−3.8, the left plots show the Reynolds stress profiles without shifting virtual origin, and the right plots show the collapse of the profile with a reference case after shifting the virtual origin. Dashed lines show the slope $1 - z^+/Re_\tau$ both before and after the shift. To investigate the effect of virtual origin across all solidity sets, all cases are matched and collapsed in a similar fashion.

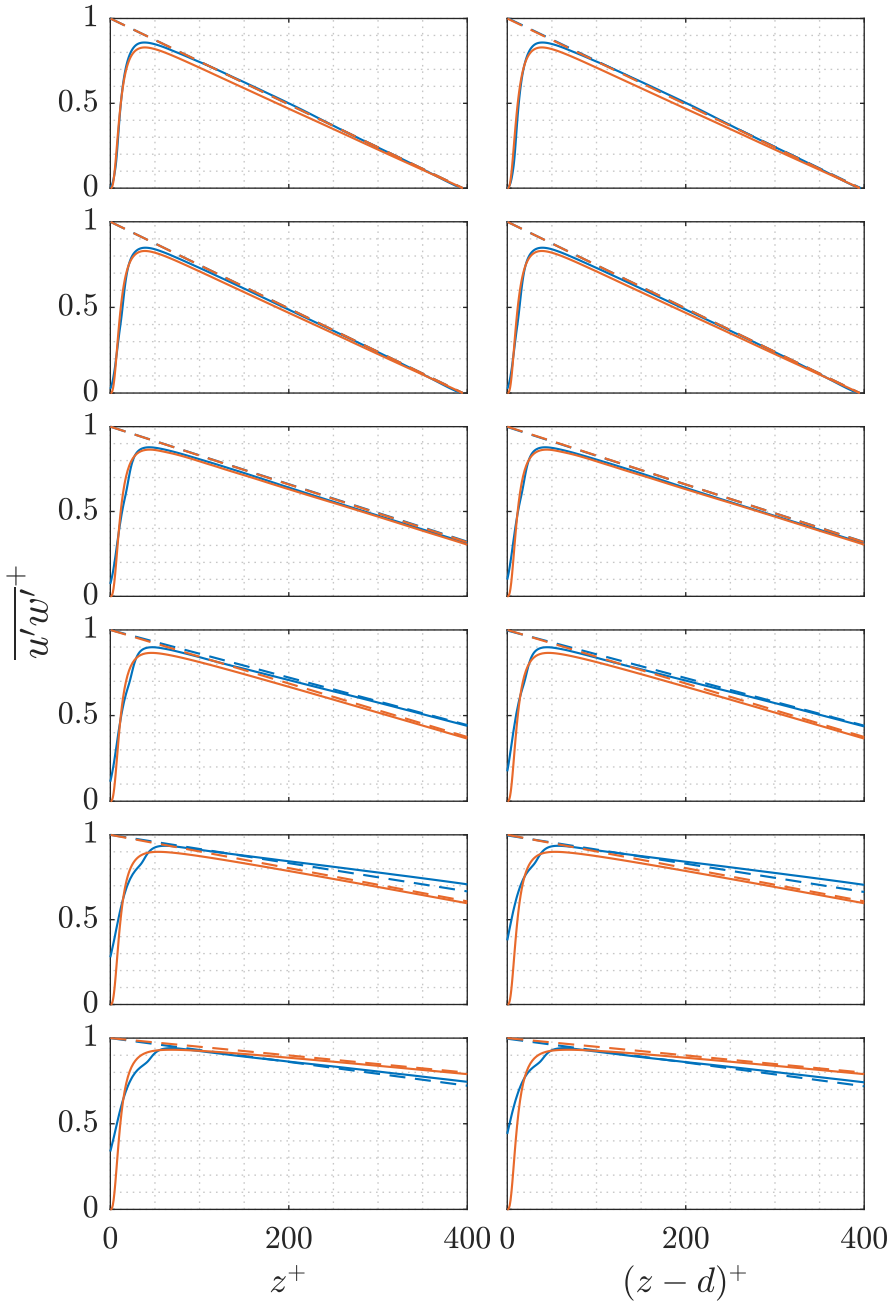

Figure 3.6: Calculation of virtual origin for low solidity cases, $\Lambda = 0.09$. Roughness Reynolds number, k^+, increases from top to bottom. Left column shows the Reynolds stress profiles, $\overline{u'w'}^+$, with the mean roughness height as the origin, and the right column shows the profiles with the virtual origin as the origin. The virtual origin is obtained by collapsing the current rough-wall profiles (—) with smooth-wall data (—) at matching or similar friction Reynolds number taken from Abe *et al.* (2001, 2004); Kozuka *et al.* (2009). Dashed lines show the slope $1 - z^+/Re_\tau$ both before and after the shift.

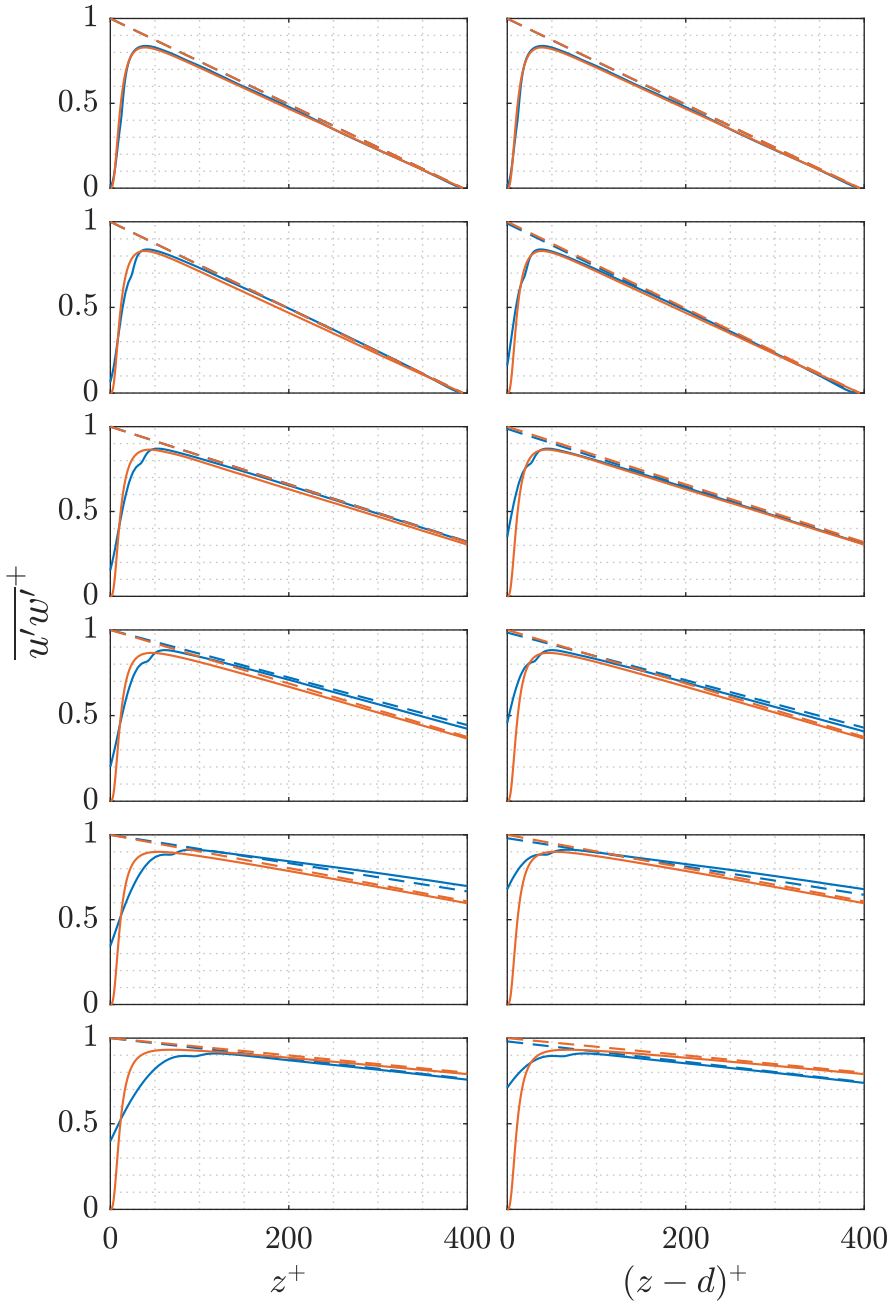

Figure 3.7: Calculation of virtual origin for medium solidity cases, $\Lambda = 0.18$. Roughness Reynolds number, k^+, increases from top to bottom. Left column shows the Reynolds stress profiles, $\overline{u'w'}^+$, with the mean roughness height as the origin, and the right column shows the profiles with the virtual origin as the origin. The virtual origin is obtained by collapsing the current rough-wall profiles (—) with smooth-wall data (—) at matching or similar friction Reynolds number taken from Abe *et al.* (2001, 2004); Kozuka *et al.* (2009). Dashed lines show the slope $1 - z^+/Re_\tau$ both before and after the shift.

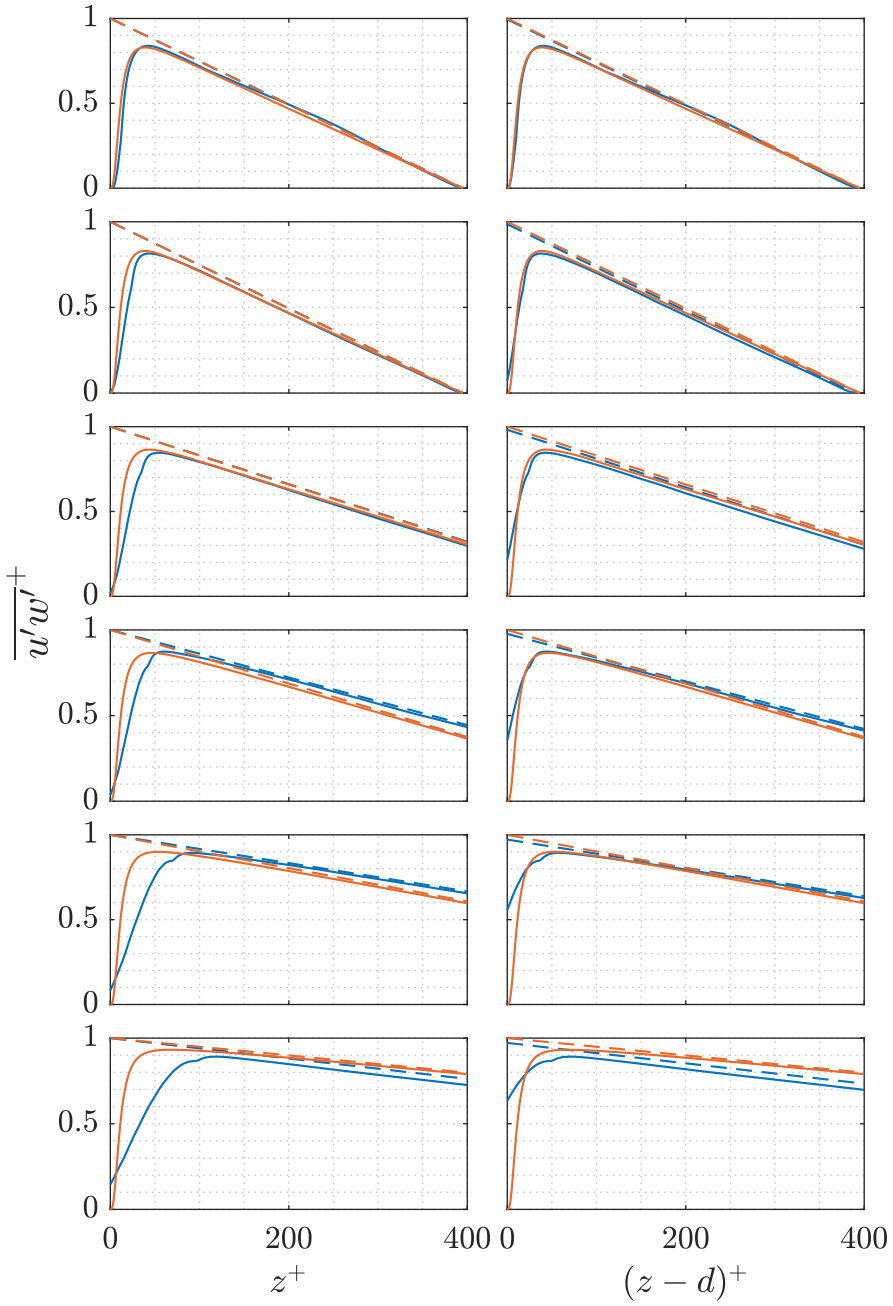

Figure 3.8: Calculation of virtual origin for high solidity cases, $\Lambda = 0.36$. Roughness Reynolds number, k^+, increases from top to bottom. Left column shows the Reynolds stress profiles, $\overline{u'w'}^+$, with the mean roughness height as the origin, and the right column shows the profiles with the virtual origin as the origin. The virtual origin is obtained by collapsing the current rough-wall profiles (—) with smooth-wall data (—) at matching or similar friction Reynolds number taken from Abe *et al.* (2001, 2004); Kozuka *et al.* (2009). Dashed lines show the slope $1 - z^+/Re_\tau$ both before and after the shift.

Figure 3.9 shows that with increasing roughness height k^+, the ratio d/k increases and tends to approach a constant value in the fully rough regime. For the low solidity set, $d/k < 0$ for $k^+ < 10$, suggesting that the virtual origin shifts below the mean roughness height for very low roughness height. With increasing k^+, for low solidity cases $d/k \approx 0.1$, meaning that the virtual origin shifts to roughly 55% of the mean roughness height when measured from the bottom of the trough. For the medium and high solidity cases, this value goes up to 67% and 75% respectively, suggesting that increasing solidity shifts the virtual origin more towards the roughness crest. This is consistent with the discussion in Section 3.1, as with $\Lambda \to \infty$, the virtual origin will approach the crest, hence making the roughness behave like a smooth wall at the crest.

Figure 3.10 shows the velocity and temperature profiles for a single case, H94_334, before and after accounting for the shift in virtual origin, and Figure 3.14 shows the profiles for all solidity sets for a fixed roughness height, $k^+ = 40$, after shifting the virtual origin. Figures 3.11, 3.12, and 3.13 show individual solidity sets plotted with the virtual origin taken into account, where the insets in (*a, b*) now show a wider plateau, making it easier to calculate the roughness functions in the subsequent section.

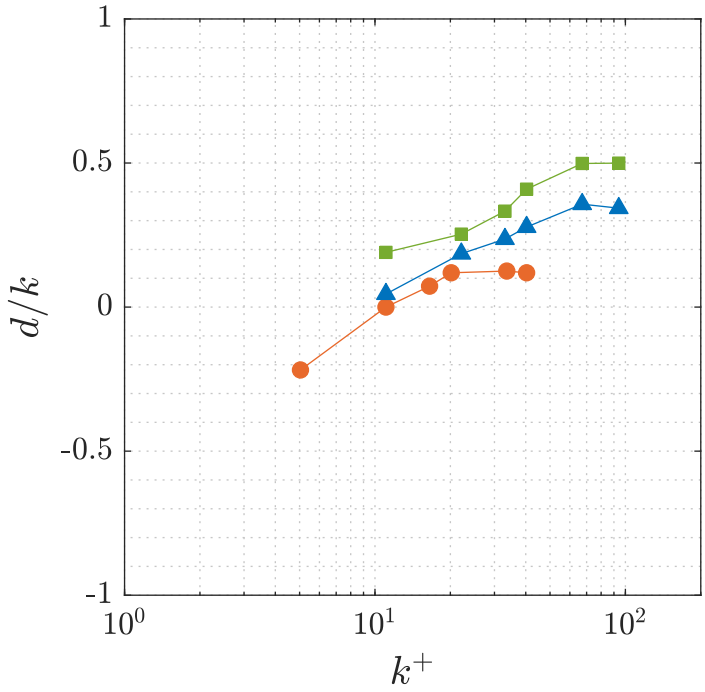

Figure 3.9: Ratio of the virtual origin shift to mean roughness height, d/k, against roughness height, k^+. Symbols: (●) low solidity, $\Lambda = 0.09$; (▲) medium solidity, $\Lambda = 0.18$; (■) high solidity, $\Lambda = 0.36$.

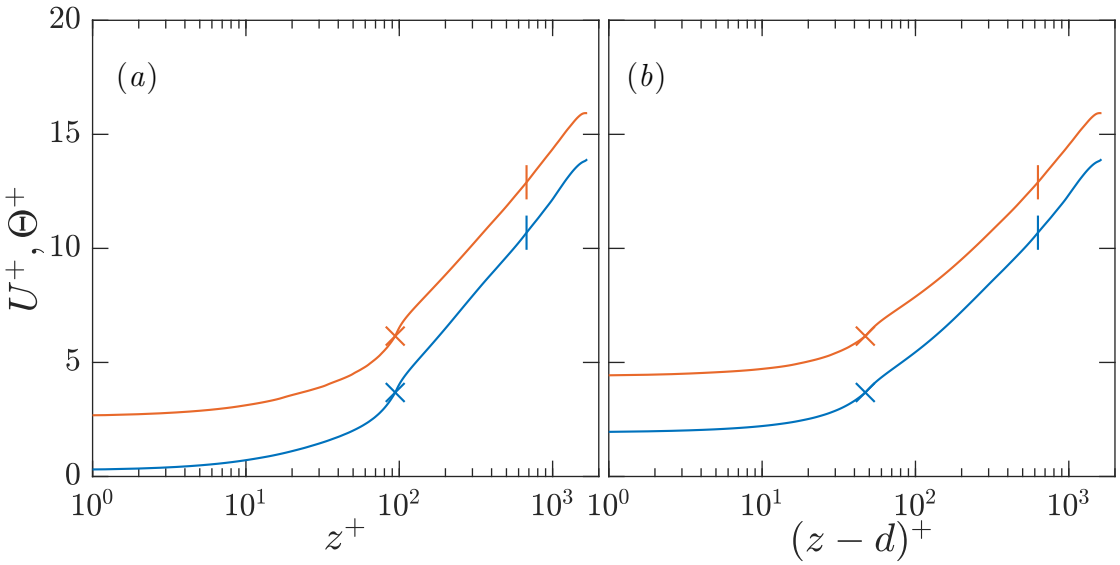

Figure 3.10: (—) Velocity and (—) temperature profiles (a) before and (b) after virtual origin shift for a single case, H94_334.

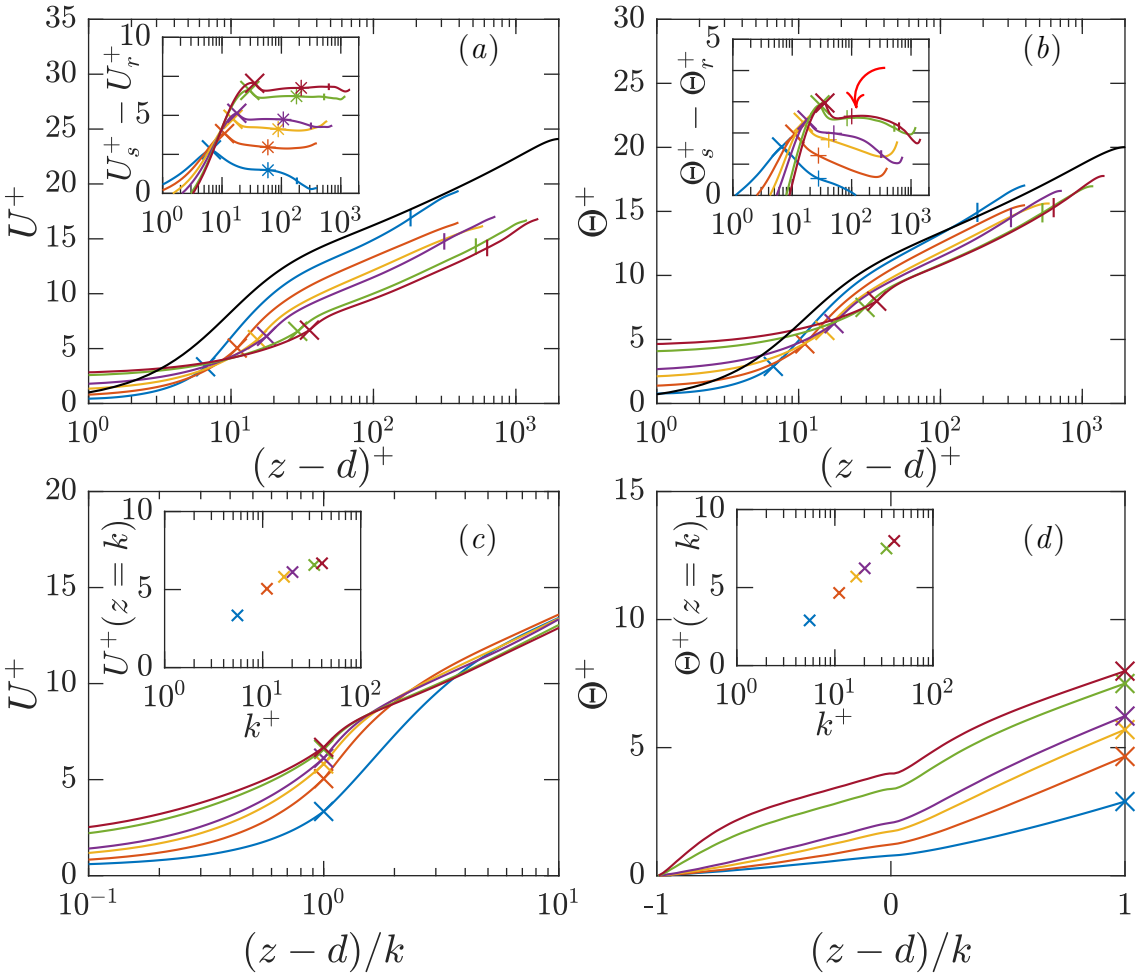

Figure 3.11: (a) Mean velocity and (b) mean temperature profiles for rough-wall open channels for low solidity, $\Lambda = 0.09$, with the virtual origin as the new origin. Roughness Reynolds number increases from top to bottom. Black solid lines are the reference smooth-wall profiles from (a) Bernardini *et al.* (2014), and (b) Pirozzoli *et al.* (2016). Insets show the roughness functions ($U_s^+ - U_r^+$, $\Theta_s^+ - \Theta_r^+$) against wall-normal location, $(z-d)^+$, where (U_s^+, Θ_s^+) are the reference smooth-wall profiles and (U_r^+, Θ_r^+) are the current rough-wall profiles. Rough-wall (c) velocity and (d) temperature profiles against $(z-d)/k$. Roughness crest velocity and temperature is plotted against k^+ in the insets of (c) and (d) respectively. Colours and symbols: (—) L06_079; (—) L11_157; (—) L17_235; (—) L20_286; (—) L34_477; (—) L40_573; ($\times$) roughness crest; (|) critical channel height, z_c^+; ($*$) calculation height of ΔU^+, $(z-d) = 0.15h$; ($+$) calculation height of $\Delta\Theta^+$, $(z-d) = 0.07h$, where the plateau region is marked with red arrow.

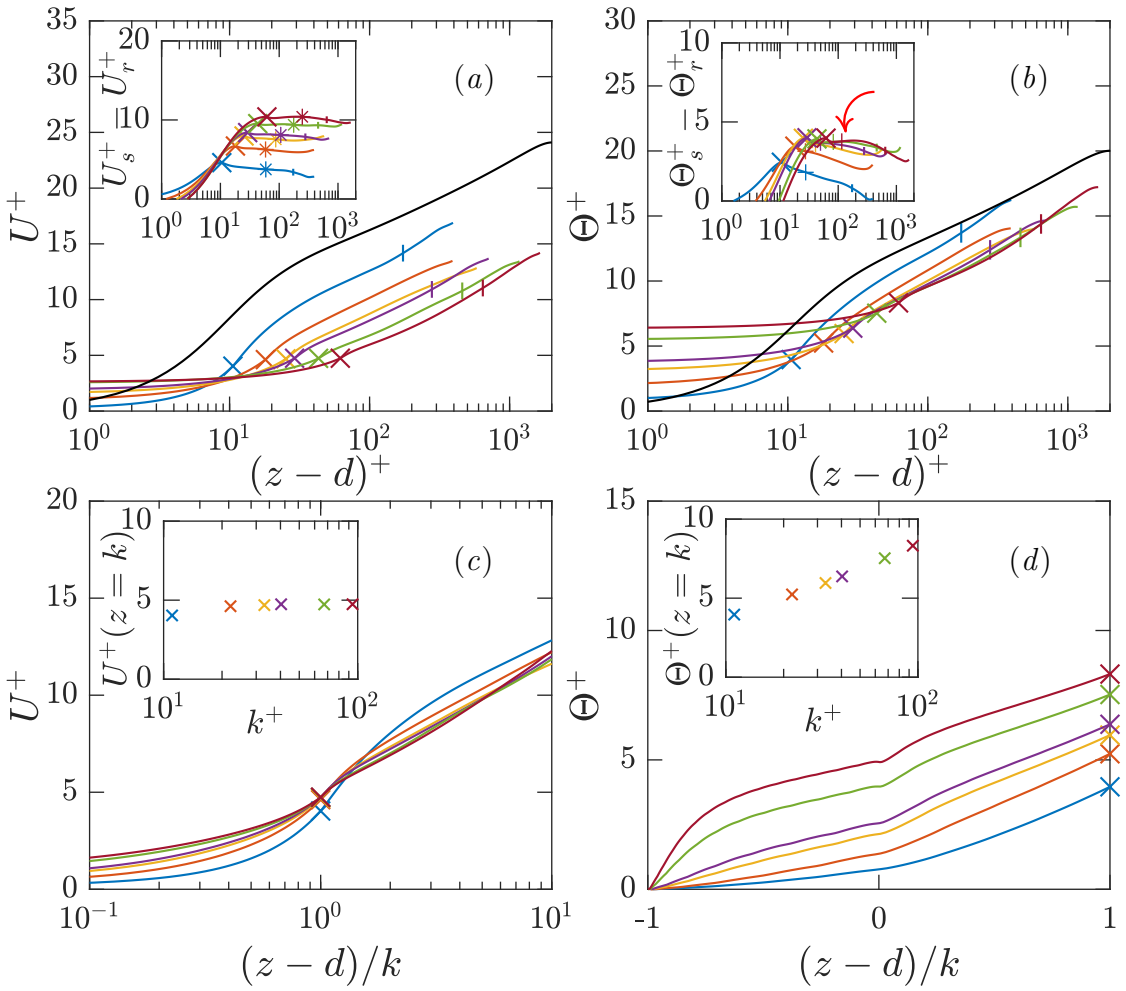

Figure 3.12: (a) Mean velocity and (b) mean temperature profiles for rough-wall open channels for medium solidity, $\Lambda = 0.18$, with the virtual origin as the new origin. Roughness Reynolds number increases from top to bottom. Black solid lines are the reference smooth-wall profiles from (a) Bernardini *et al.* (2014), and (b) Pirozzoli *et al.* (2016). Insets show the roughness functions ($U_s^+ - U_r^+$, $\Theta_s^+ - \Theta_r^+$) against wall-normal location, $(z-d)^+$, where (U_s^+, Θ_s^+) are the reference smooth-wall profiles and (U_r^+, Θ_r^+) are the current rough-wall profiles. Rough-wall (c) velocity and (d) temperature profiles against $(z-d)/k$. Roughness crest velocity and temperature is plotted against k^+ in the insets of (c) and (d) respectively. Colours and symbols: (—) M11_079; (—) M22_157; (—) M33_235; (—) M40_286; (—) M67_477; (—) M94_668; (×) roughness crest; (|) critical channel height, z_c^+; (∗) calculation height of ΔU^+, $(z-d) = 0.15h$; (+) calculation height of $\Delta\Theta^+$, $(z-d) = 0.07h$, where the plateau region is marked with red arrow.

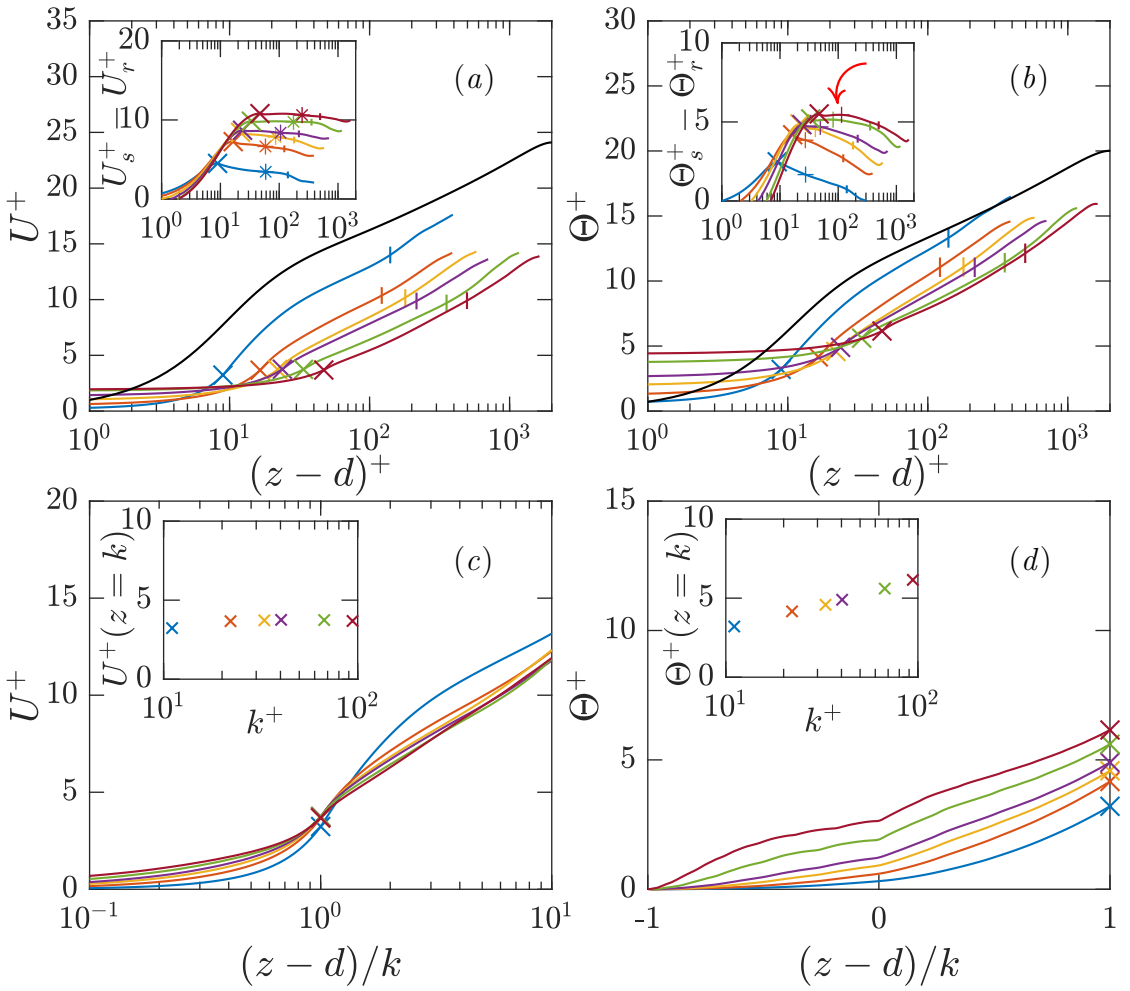

Figure 3.13: (a) Mean velocity and (b) mean temperature profiles for rough-wall open channels for high solidity, $\Lambda = 0.36$, with the virtual origin as the new origin. Roughness Reynolds number increases from top to bottom. Black solid lines are the reference smooth-wall profiles from (a) Bernardini *et al.* (2014), and (b) Pirozzoli *et al.* (2016). Insets show the roughness functions ($U_s^+ - U_r^+$, $\Theta_s^+ - \Theta_r^+$) against wall-normal location, $(z-d)^+$, where (U_s^+, Θ_s^+) are the reference smooth-wall profiles and (U_r^+, Θ_r^+) are the current rough-wall profiles. Rough-wall (c) velocity and (d) temperature profiles against $(z-d)/k$. Roughness crest velocity and temperature is plotted against k^+ in the insets of (c) and (d) respectively. Colours and symbols: (—) H11_039; (—) H22_079; (—) H33_117; (—) H40_143; (—) H67_239; (—) H94_334; (×) roughness crest; (|) critical channel height, z_c^+; (∗) calculation height of ΔU^+, $(z-d) = 0.15h$; (+) calculation height of $\Delta\Theta^+$, $(z-d) = 0.07h$, where the plateau region is marked with red arrow.

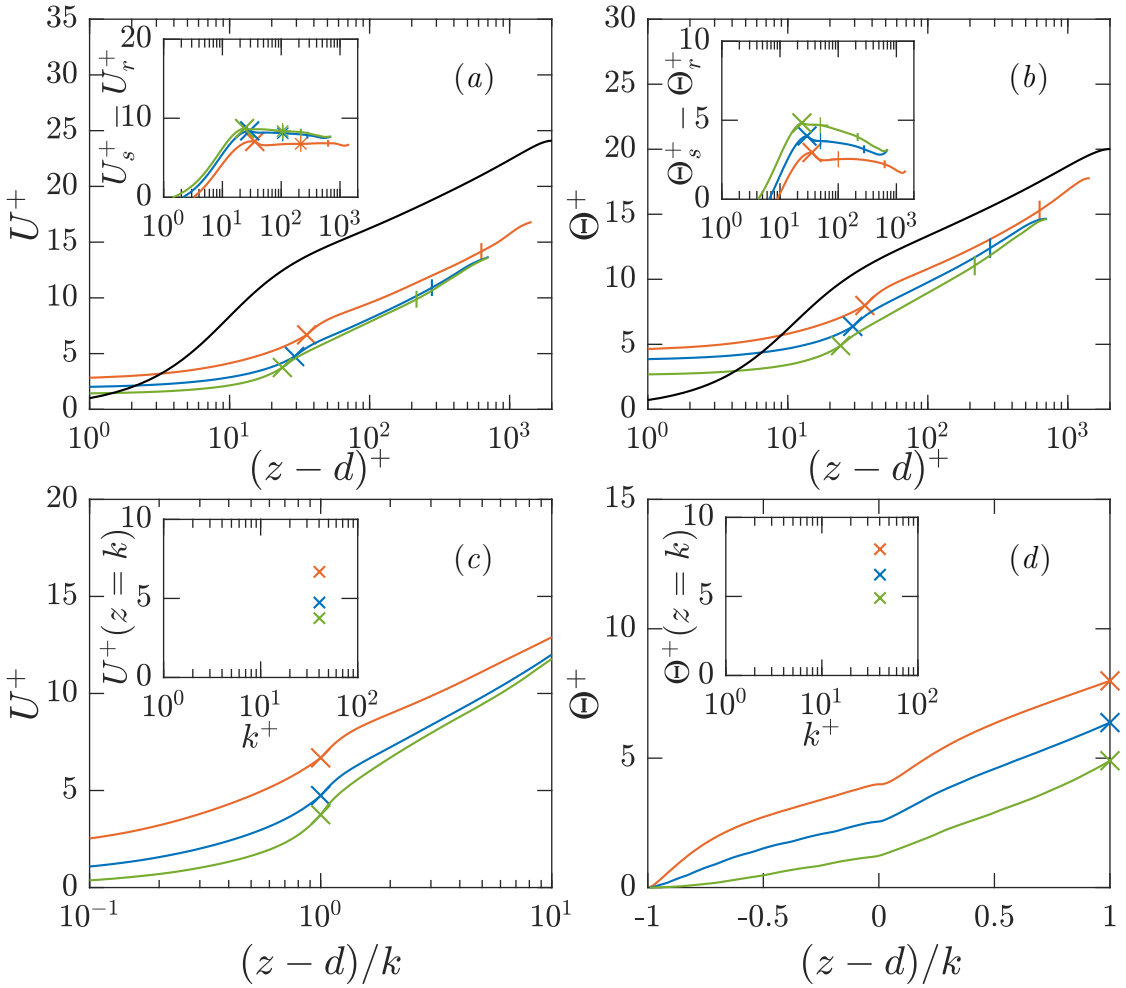

Figure 3.14: (a) Mean velocity and (b) mean temperature profiles for rough-wall open channels for all solidity sets at fixed roughness height, $k^+ = 40$, with the virtual origin as the new origin. Black solid lines are the reference smooth-wall profiles from (a) Bernardini *et al.* (2014), and (b) Pirozzoli *et al.* (2016). Insets show the roughness functions ($U_s^+ - U_r^+$, $\Theta_s^+ - \Theta_r^+$) against wall-normal location, $(z-d)^+$, where (U_s^+, Θ_s^+) are the reference smooth-wall profiles and (U_r^+, Θ_r^+) are the current rough-wall profiles. Rough-wall (c) velocity and (d) temperature profiles against $(z-d)/k$. Roughness crest velocity and temperature is plotted against k^+ in the insets of (c) and (d) respectively. Colours and symbols: (—) L40_573; (—) M40_286; (—) H40_143; (×) roughness crest; (|) critical channel height, z_c^+; $(*)$ calculation height of ΔU^+, $(z-d) = 0.15h$; (+) calculation height of $\Delta\Theta^+$, $(z-d) = 0.07h$.

3.3 Roughness functions

Case	Re_τ	k^+	ΔU^+_{ns}	$\Delta\Theta^+_{ns}$	ΔU^+_{vs}	$\Delta\Theta^+_{vs}$
L06_079	395	5.53	1.44	0.41	1.49	0.54
L11_157	395	11.06	2.96	1.27	2.96	1.27
L17_235	590	16.52	4.15	1.87	4.12	1.78
L20_286	720	20.16	4.79	2.11	4.73	1.99
L34_477	1200	33.60	6.28	2.58	6.22	2.47
L40_573	1440	40.32	6.82	2.63	6.76	2.53
M11_079	395	11.06	3.77	1.88	3.75	1.81
M22_157	395	22.12	6.45	3.75	6.26	3.15
M33_235	590	33.04	7.78	4.24	7.55	3.61
M40_286	720	40.32	8.37	4.35	8.10	3.68
M67_477	1200	67.20	9.78	4.44	9.39	3.73
M94_668	1680	94.08	10.76	4.42	10.40	3.77
H11_039	395	11.06	3.53	1.97	3.44	1.67
H22_079	395	22.12	6.92	4.70	6.65	3.85
H33_117	590	33.04	8.20	5.50	7.85	4.55
H40_143	720	40.32	8.81	5.73	8.38	4.69
H67_239	1200	67.20	10.30	6.25	9.76	5.15
H94_334	1680	94.08	11.21	6.50	10.62	5.45

Table 3.2: Roughness functions for all cases before and after virtual origin shift. (ΔU^+_{ns}, $\Delta\Theta^+_{ns}$) and (ΔU^+_{vs}, $\Delta\Theta^+_{vs}$) are the roughness functions before and after accounting for virtual origin shift.

The momentum and temperature roughness functions (ΔU^+, $\Delta\Theta^+$) across all solidity sets are tabulated in Table 3.2. For all cases, the momentum roughness function is taken at $z = 0.15h + d$ before and after shifting the virtual origin. Because of the constant drop in the $\Theta^+_s - \Theta^+_r$ profiles seen in the insets of Figure 3.11(b), 3.12(b), and 3.13(b), it is difficult to calculate the temperature roughness functions. MacDonald *et al.* (2019) calculated all the roughness functions at their critical channel height, $z^+_{c,M}$, using matched smooth-wall simulations. Such an ap-

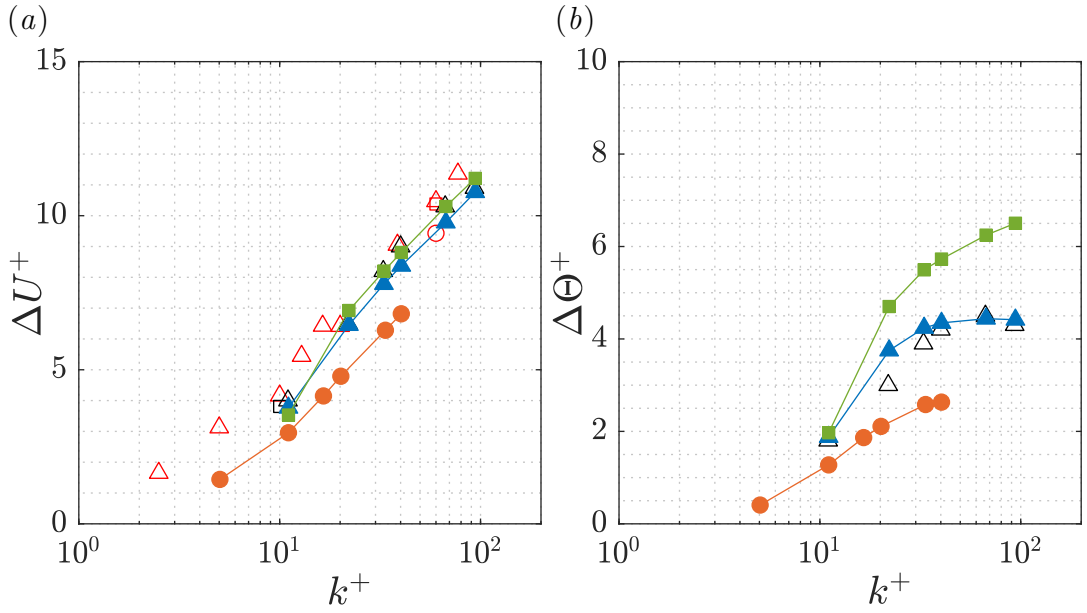

Figure 3.15: Roughness functions for momentum (left) and temperature (right) without virtual origin shift. Symbols: (●) low solidity, $\Lambda = 0.09$; (▲) medium solidity, $\Lambda = 0.18$; (■) high solidity, $\Lambda = 0.36$; (○) Chan *et al.* (2018), $\Lambda = 0.09$; (△) Chan *et al.* (2018), $\Lambda = 0.18$; (□) Chan *et al.* (2018), $\Lambda = 0.36$; (△) MacDonald *et al.* (2019), $\Lambda = 0.18$; (□) MacDonald *et al.* (2016), $\Lambda = 0.36$.

proach can introduce errors in this case, considering that the reference smooth-wall profile is not matched to the current rough-wall cases. However, a closer observation shows that the $\Theta_s^+ - \Theta_r^+$ profiles in the insets of Figure 3.11(b), 3.12(b), and 3.13(b) show a small plateau (marked with red arrow) above the roughness crest, at $(z - d) \approx 0.07h$. This plateau is more noticeable for the higher k^+ cases for all solidity sets. Thus, the temperature roughness function is taken at $z = 0.07h + d$ before and after shifting the virtual origin.

Figure 3.15 shows the roughness functions calculated before taking the virtual origin shift into account, compared to the reported roughness functions of Chan *et al.* (2015) and MacDonald *et al.* (2016, 2019). It is already shown that it is possible to reproduce the roughness functions reported by MacDonald *et al.*

(2019) in Section 2.5. However, here the roughness functions are recalculated at $(z-d) = 0.15h$ and $(z-d) = 0.07h$ for the momentum and temperature respectively. This leads to some disagreements among the current study and the reference cases, particularly because all these studies use different methods to calculate the roughness functions. Nevertheless, ΔU^+ across all solidity sets of the current study shows the logarithmic behaviour, consistent with the fully rough regime. This can be noticed more clearly for the medium and high solidity sets, with the low solidity set slowly approaching the fully rough regime too. An increase in solidity creates a greater change in ΔU^+ for low-to-medium solidity than for medium-to-high solidity, as discussed in the preliminary observations in Section 3.1. As for the temperature, the overall tendency of the temperature functions approaching a constant value in the fully-rough regime can be observed, but with increasing solidity, $\Delta\Theta^+$ seems to increase too. Unlike ΔU^+, $\Delta\Theta^+$ does not seem to show a greater change for low-to-medium solidity than for medium-to-high solidity.

For $\Lambda \to \infty$, the wall becomes smooth. However, this also means that the height of the channel reduces by k^+. In this regime, the temperature difference becomes zero, but because the channel now has a shorter height, the temperature difference of zero is only meaningful when compared against a channel of the same height.

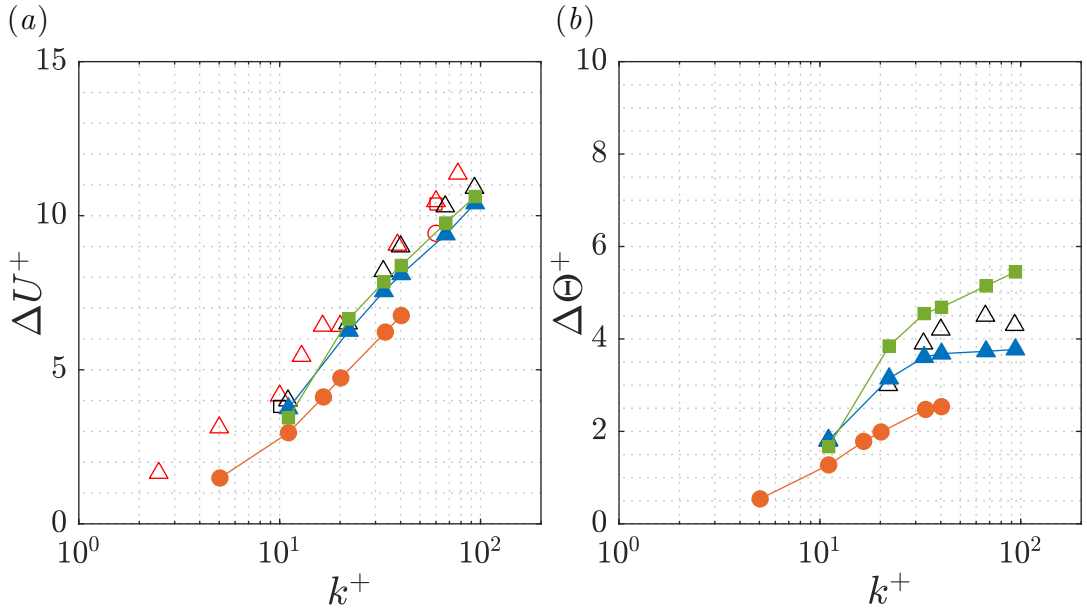

Figure 3.16: Roughness functions for momentum (a) and temperature (b) with virtual origin shift. Symbols: (●) low solidity, $\Lambda = 0.09$; (▲) medium solidity, $\Lambda = 0.18$; (■) high solidity, $\Lambda = 0.36$; (○) Chan *et al.* (2018), $\Lambda = 0.09$; (△) Chan *et al.* (2018), $\Lambda = 0.18$; (□) Chan *et al.* (2018), $\Lambda = 0.36$; (△) MacDonald *et al.* (2019), $\Lambda = 0.18$; (□) MacDonald *et al.* (2016), $\Lambda = 0.36$.

The virtual origin is shifted and the roughness functions are calculated at $(z - d) = 0.15h$ for velocity and $(z - d) = 0.07h$ for temperature. A decrease in roughness functions is seen (Figure 3.16) for both momentum and temperature. The momentum roughness function now sits even lower compared to the reference roughness function data than it was without the virtual origin shift, yet still follows the logarithmic fit in the fully-rough regime.

Figure 3.17 shows the velocity and temperature roughness functions against solidity. For $k^+ \approx 11$, the velocity roughness functions agree with the findings of MacDonald *et al.* (2016), where the trend is that ΔU^+ increases with increasing solidity for $\Lambda < 0.15$ and decreases for $\Lambda > 0.15$, although in the present study, a more appropriate value for this transition can be seen as $\Lambda = 0.18$ (Figure 3.17(a)).

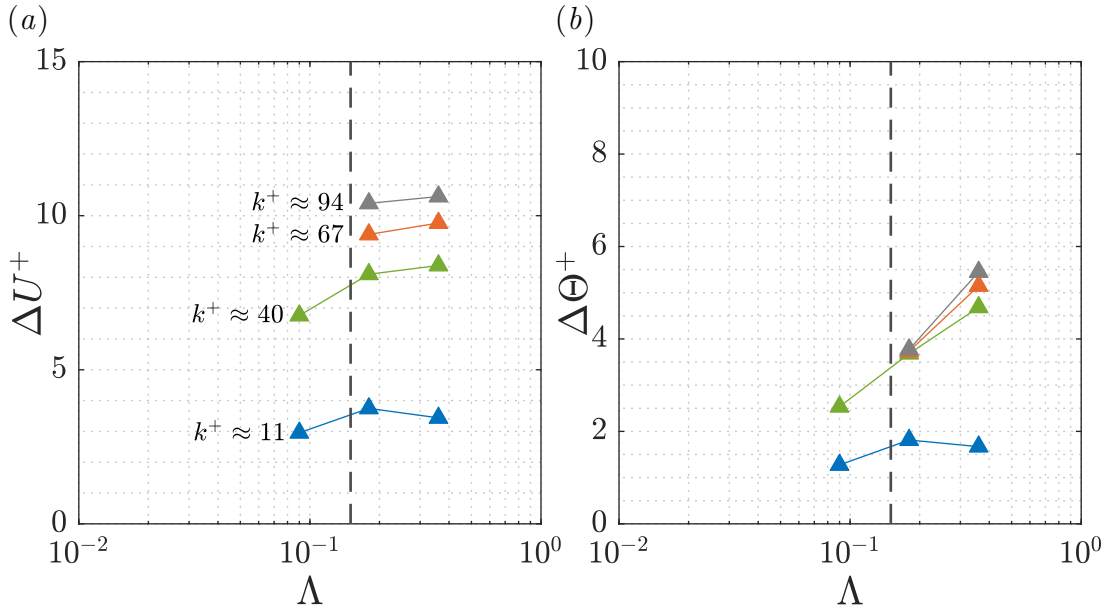

Figure 3.17: Roughness functions for momentum (a) and temperature (b) against solidity, Λ. Symbols: (▲) $k^+ \approx 11$; (▲) $k^+ \approx 40$; (▲) $k^+ \approx 67$; (▲) $k^+ \approx 94$.

For higher k^+ cases, however, this trend is absent. The increase in ΔU^+ for $\Lambda < 0.18$ is more prominent, but ΔU^+ slightly increases for $\Lambda > 0.18$ too. The temperature roughness functions in Figure 3.17(b) show a slight decrease for $k^+ \approx 11$, but higher k^+ values show a noticeable increase in $\Delta\Theta^+$ with increasing solidity. At $\Lambda = 0.18$, all the temperature roughness functions of higher k^+ cases form a cluster, signifying they have approached a constant. For $\Lambda = 0.36$, the $\Delta\Theta^+$ values seem to be getting closer together and should eventually approach a constant.

With these roughness functions, the current data is collapsed onto the fully rough asymptote of Nikuradse (1933) to establish the equivalent sand-grain roughness, k_s/k. For the same roughness geometry as the medium solidity set, Chan *et al.* (2015) found $k_s/k = 4.1$ compared to $k_s/k = 3$ found in this study. Chan *et al.* (2015) performed pipe flow simulations, and calculated the roughness functions at 50 wall units above the roughness crest considering negligible virtual origin effects.

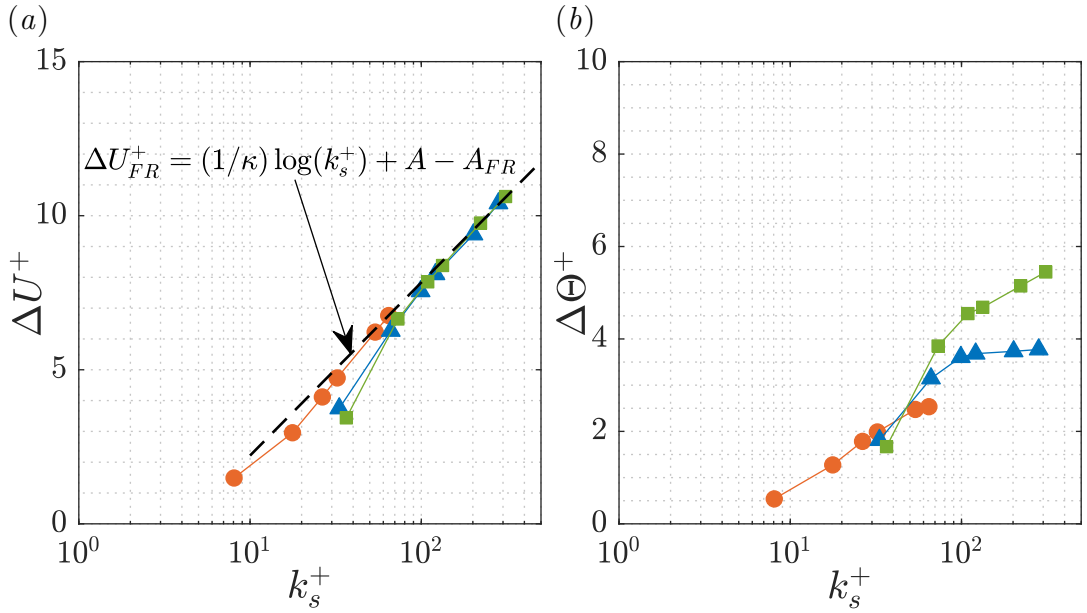

Figure 3.18: Roughness functions for momentum (a) and temperature (b) with virtual origin shift, plotted against equivalent sand-grain roughness, k_s^+. Symbols: (●) low solidity, $\Lambda = 0.09$; (▲) medium solidity, $\Lambda = 0.18$; (■) high solidity, $\Lambda = 0.36$.

They also used $\kappa = 0.40$ and $A = 5.3$ for pipe flow, compared to $\kappa = 0.41$ and $A = 5.1$ for channel flow used in this study. All these factors may have contributed to the difference in the value of k_s/k. For the low and high solidity sets, k_s/k is found to be 1.6 and 3.3 respectively. Note that $k_s/k = 1.6$ for the low solidity set has been found by collapsing the ΔU^+ of $k^+ \approx 40$ on to the fully rough asymptote. This roughness height is most likely to be still in the upper limits of transitionally rough regime, and the true value of k_s/k for the low solidity could thus be higher. The roughness functions are again plotted in Figure 3.18 against the equivalent sand-grain roughness, k_s^+. While the velocity roughness functions in Figure 3.18(a) are collapsed to the fully rough asymptote, the temperature roughness functions in Figure 3.18(b) show an increase for increasing solidity at similar k_s^+ without any discernible trend.

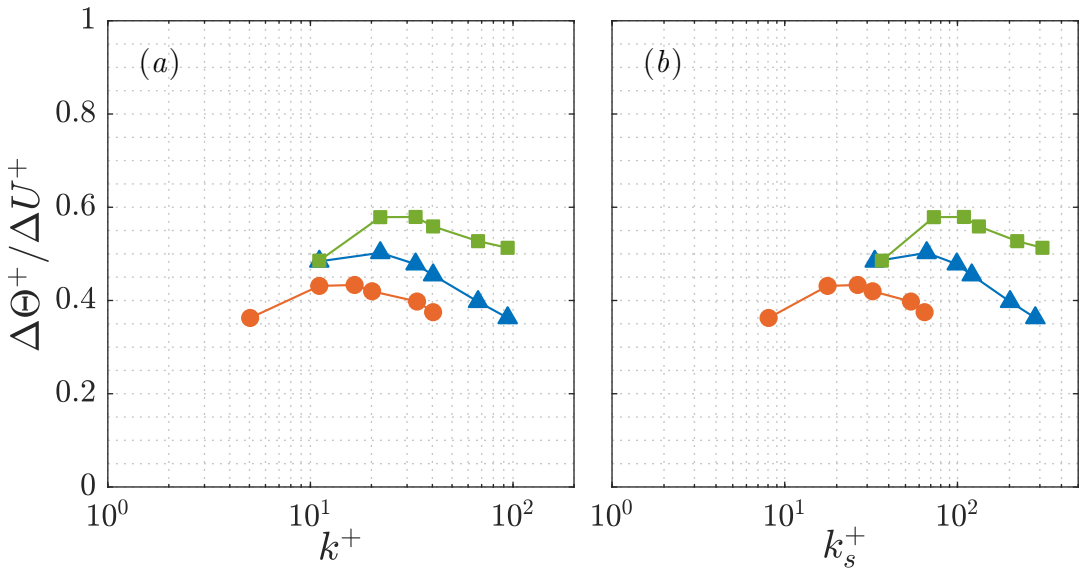

Figure 3.19: Ratio of temperature and momentum roughness functions against (a) mean roughness height, k^+, and (b) equivalent sand-grain roughness height, k_s^+. Symbols: (●) low solidity, $\Lambda = 0.09$; (▲) medium solidity, $\Lambda = 0.18$; (■) high solidity, $\Lambda = 0.36$.

Figure 3.19 shows the plot of $\Delta\Theta^+/\Delta U^+$ against k^+ and k_s^+. It is observed that this ratio increases in the transitionally rough regime where it peaks, and then starts decreasing as the flow starts approaching the fully rough state. This is true across all solidity sets, and signifies that $\Delta\Theta^+$ has either become constant or has started decreasing in the fully rough regime while ΔU^+ has continued increasing. This increase in ΔU^+ is expected when the flow has reached the fully rough state because of the increase in pressure drag. Here it seems that the temperature roughness function $\Delta\Theta^+$ is approaching a constant value, as found by MacDonald *et al.* (2019). However, this constant seems to be dependent on the solidity, as higher solidity can be seen to approach a constant higher than that of medium or low solidity.

3.4 Visualisations

The following figures show the instantaneous streamwise velocity and temperature contours for all cases across all solidity sets taken in the $x - z$ plane. The viscous and thermal diffusive sublayers are highlighted with white contour lines at $u^+ = 4$ and $\theta^+ = 4$, and the zero velocity (recirculation) regions are highlighted with black contour lines. For all the plots, flow is from left to right.

It can be observed that for all solidity sets and low k^+ cases, the flow near the wall forms thin sublayers, and the roughness elements are submerged in these sublayers. The temperature above the thermal sublayer is well-mixed, and the temperature gradient within the sublayer is responsible for the heat transfer. With increasing k^+, the viscous sublayer mostly occupies the areas around the roughness crest, with the recirculation regions (black contour line) getting larger. As for the thermal sublayer, it thickens in the transitionally rough regime, and then starts to conform to the shape of the roughness elements. This can be compared to a smooth wall with increased wetted area. For a wall with wall location z_w, streamwise and spanwise length of L_x and L_y respectively, the ratio between the wetted area, A_W, and the total plan area, A_T can be written as,

$$\frac{A_W}{A_T} = \frac{1}{L_x L_y} \int_0^{L_y} \int_0^{L_x} \sqrt{1 + \left(\frac{\partial z_w}{\partial x}\right)^2 + \left(\frac{\partial z_w}{\partial y}\right)^2} \, \mathrm{d}x \, \mathrm{d}y \tag{3.1}$$

For the roughness studied here, it can be shown that $\frac{A_W}{A_T} = 1.048$ for low solidity, $\frac{A_W}{A_T} = 1.178$ for medium solidity, and $\frac{A_W}{A_T} = 1.586$ for high solidity. While this increase in wetted area may not alone explain the increase in heat transfer, it is most likely a contributing factor.

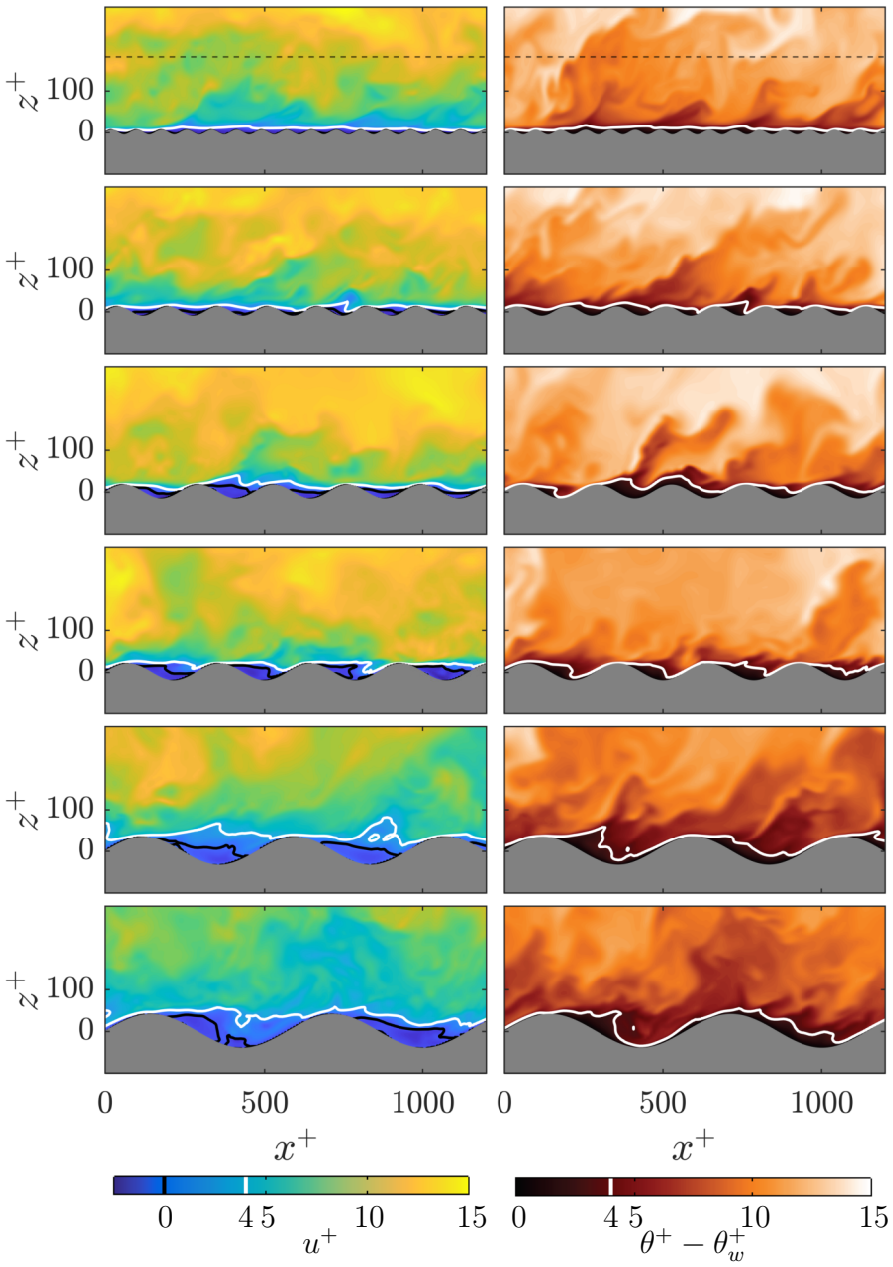

Figure 3.20: Instantaneous velocity (left) and temperature (right) contours for low solidity, $\Lambda = 0.09$. Roughness Reynolds number, k^+, increases from top to bottom. Viscous and thermal diffusive sublayers are highlighted with white contour lines at $u^+ = 4$ and $\theta^+ = 4$ respectively, and zero velocity (recirculation) regions are highlighted with black contour lines. Horizontal dashed-line shows the critical channel height, z_c^+. Flow is from left to right.

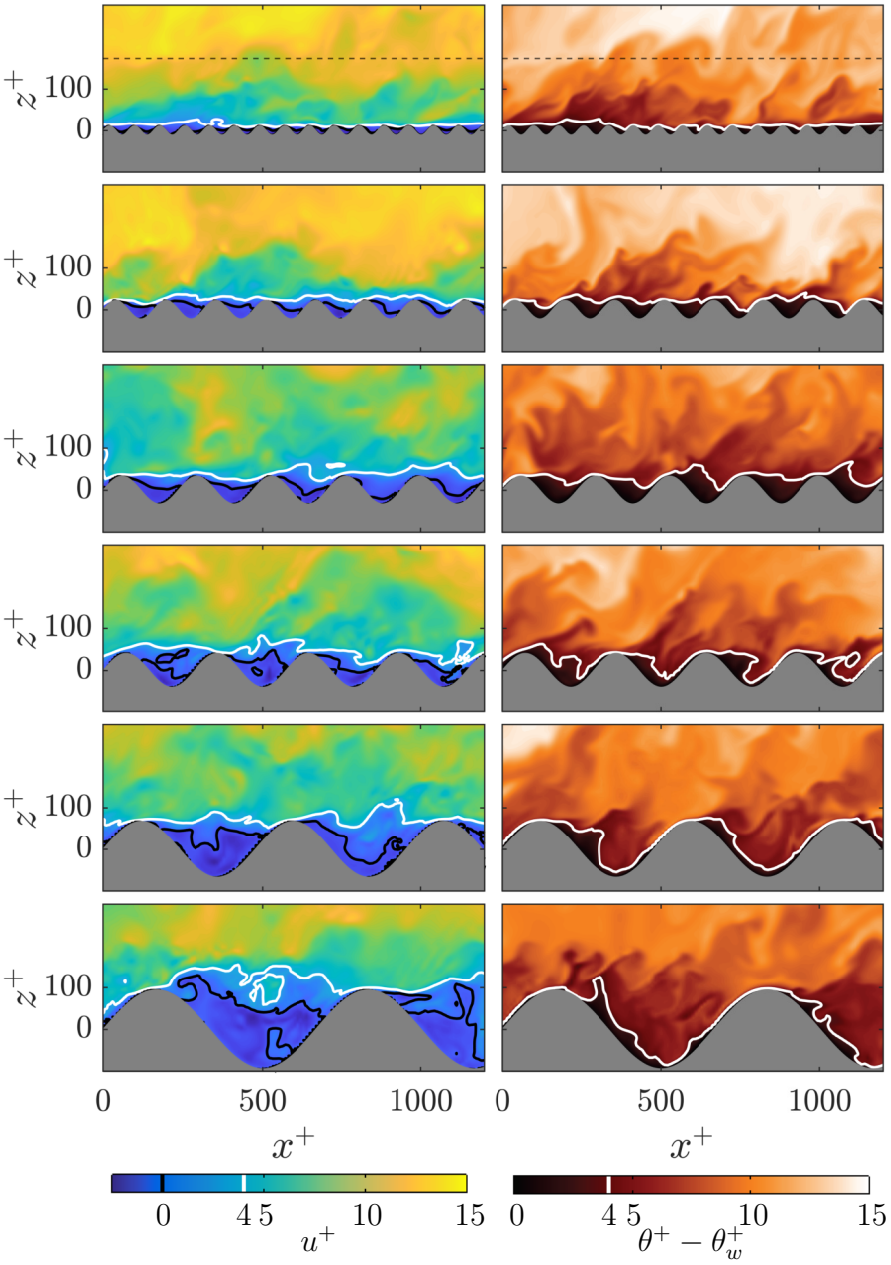

Figure 3.21: Instantaneous velocity (left) and temperature (right) contours for medium solidity, $\Lambda = 0.18$. Roughness Reynolds number, k^+, increases from top to bottom. Viscous and thermal diffusive sublayers are highlighted with white contour lines at $u^+ = 4$ and $\theta^+ = 4$ respectively, and zero velocity (recirculation) regions are highlighted with black contour lines. Horizontal dashed-line shows the critical channel height, z_c^+. Flow is from left to right.

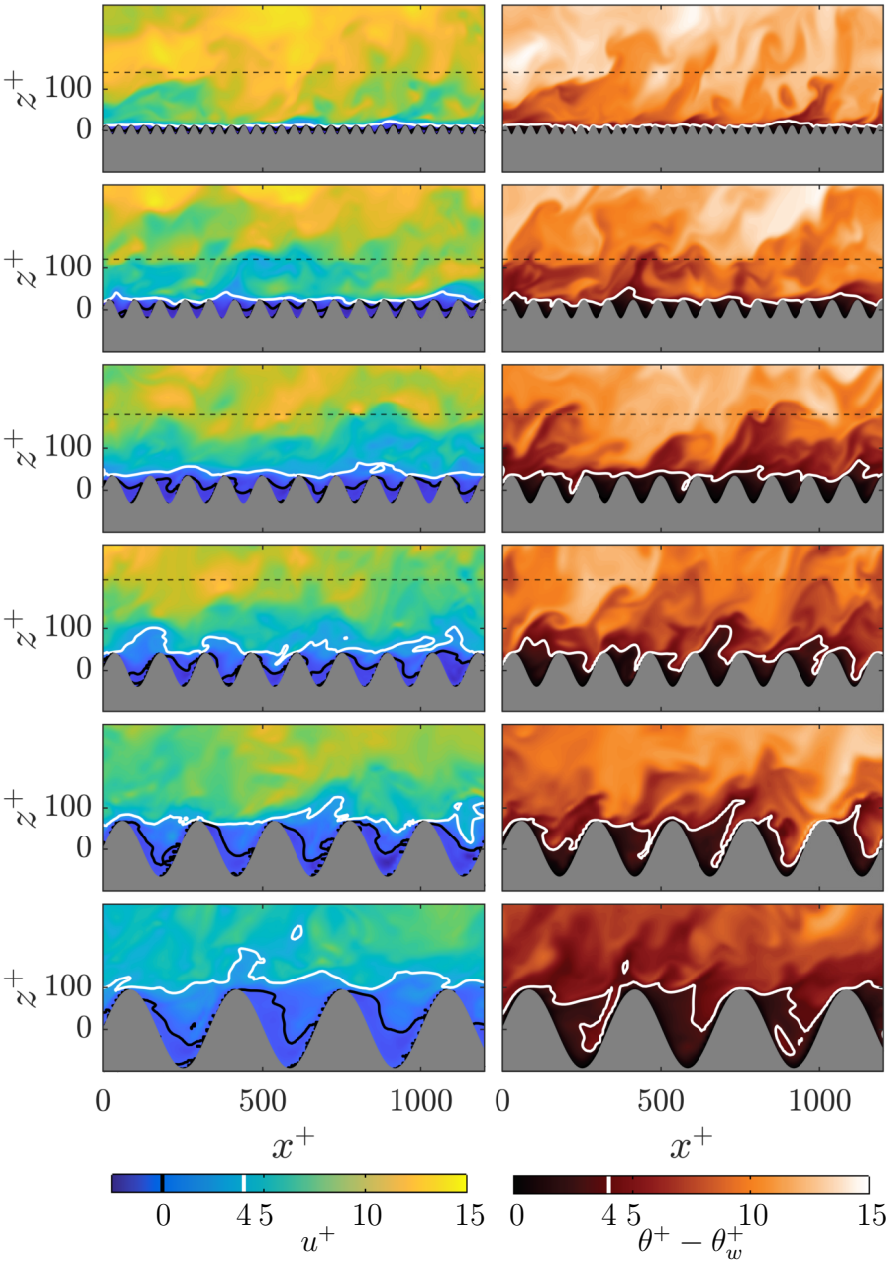

Figure 3.22: Instantaneous velocity (left) and temperature (right) contours for high solidity, $\Lambda = 0.36$. Roughness Reynolds number, k^+, increases from top to bottom. Viscous and thermal diffusive sublayers are highlighted with white contour lines at $u^+ = 4$ and $\theta^+ = 4$ respectively, and zero velocity (recirculation) regions are highlighted with black contour lines. Horizontal dashed-line shows the critical channel height, z_c^+. Flow is from left to right.

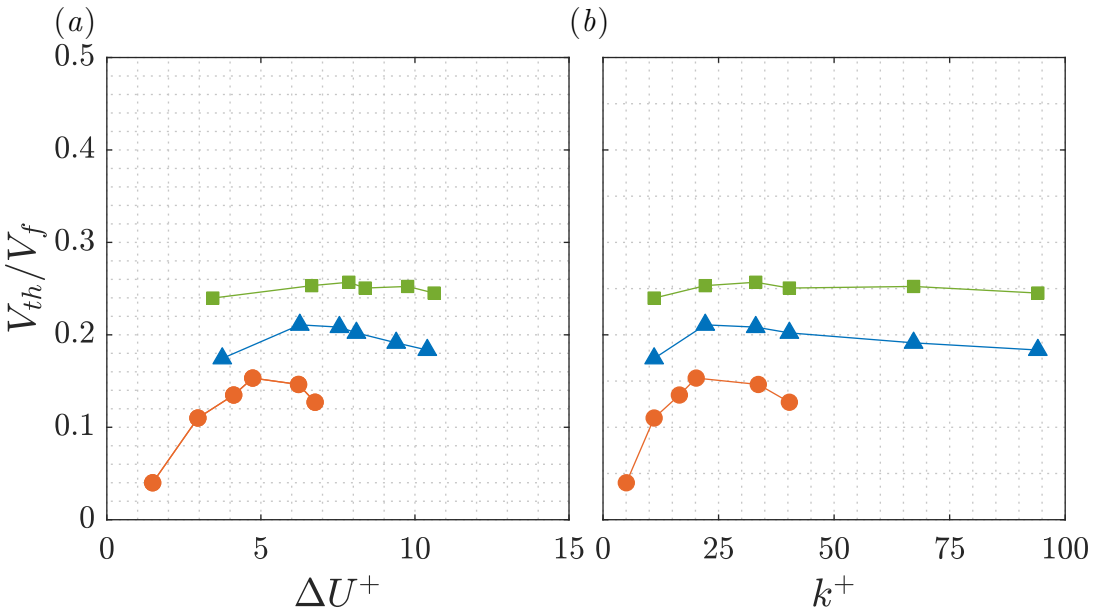

Figure 3.23: Ratio of the volume of fluid within recirculation region to the total volume of fluid from roughness crest to trough (plotted using one instantaneous snapshot) against roughness function, ΔU^+, and mean roughness height, k^+. Here, V_{th} is the total volume of fluid that lies within the recirculation region, and V_f is the total volume of fluid from the roughness peak to trough. Symbols: (●) low solidity, $\Lambda = 0.09$; (▲) medium solidity, $\Lambda = 0.18$; (■) high solidity, $\Lambda = 0.36$.

A visual inspection of the instantaneous velocity contours show an increase of recirculation regions behind the roughness elements with increasing solidity. A simple approach is taken to quantify this, where the ratio of total volume of fluid that lies within the recirculation region, V_{th}, to the total volume of fluid from the roughness crest to trough, V_f, is calculated for a single timestep. Figure 3.23 shows that for all solidity sets, this ratio increases from low k^+ up to the transitionally rough regime, and then approaches a constant where ΔU^+ (Figure 3.23(a)) as well as k^+ (Figure 3.23(b)) keep increasing. However, V_{th}/V_f increases for increasing solidity but approaches different constant values for different solidity sets. For example, in the fully rough regime, V_{th}/V_f increases by 27% from medium to high

solidity, meaning that the recirculation region is bigger in the high solidity set. For two different cases with same or similar ΔU^+, $\Delta\Theta^+$ may not be the same because of this, as a larger recirculation region will bring in more well-mixed fluid from outside the thermal sublayer and enhance heat transfer. This transportation of well-mixed fluid, together with the increase in wetted area may explain the increase in heat transfer with increasing solidity.

Chapter 4
Conclusions

This study reports DNS results for open-channel flows with three-dimensional sinusoidal roughness, with increasing viscous-scaled roughness height, k^+, and three different roughness solidities. The roughness heights across the solidity sets have been matched to investigate the effects of increasing roughness solidity on both the momentum and the heat transfer in turbulent open-channel flows. Immersed boundary method has been used here to implement the roughness geometry, and the minimal-span channel approach has been utilised in most cases to reduce the computational cost while increasing the range of friction Reynolds number, Re_τ, to cover the transitionally rough regime for all the solidity sets, and fully rough regime for the medium and high solidity cases. While the highest k^+ case for the low solidity set studied here does not quite reach the fully rough regime, it provides critical insight to the overall comparison across all solidity sets. All cases in this study have been sufficiently resolved to capture the smallest scales of turbulent motion. Mean velocity and temperature profiles for all cases have been analysed, and the roughness functions have been discussed with taking the virtual origin effects into account. Instantaneous velocity and temperature contours are also plotted to explain the behaviour of the flow at different roughness heights and solidity.

The general behaviours of the mean profiles for a turbulent flow are observed, with the velocity and the temperature approaching zero and prescribed wall temperature at the wall respectively. The well known logarithmic behaviour of the flow

away from the wall for both the velocity and temperature profiles is also observed. With increasing roughness height, k^+, a parallel downward shift in the logarithmic region of the mean profiles (when compared to the mean profiles of a smooth-wall flow) is seen, which is a well-known feature in literature. It is noticed that a higher solidity, especially for $\Lambda = 0.36$, seems to change the slope of the logarithmic region due to a change in the virtual origin.

The shift in virtual origin is calculated based on the suggestions of Luchini *et al.* (1991), which involves collapsing the Reynolds stress profiles of rough-wall cases on to that of matched or similar smooth-wall cases. This is done across all solidity sets, and the mean velocity and temperature profiles are once again plotted. The difference of smooth- and rough-wall mean profiles now has a wider plateau in the logarithmic region, making it easier in the latter sections to calculate the roughness functions. The change in virtual origin relative to the mean roughness height is also investigated, and is observed to have a lower value for low roughness height and approach a constant value at higher roughness heights. It is also found that the shift in virtual origin also increases with increasing roughness solidity.

Roughness functions for all cases both before and after accounting for the shift in virtual origin are calculated. The data was previously validated using reference data from literature. For proper comparison, the roughness functions were calculated using the approach proposed in the reference, and both the present data and the reference had good agreement. However, here a different approach is utilised in calculating both the velocity and temperature roughness functions. Using this data, equivalent sand-grain roughness for the current sinusoidal roughness at each solidity is established. It is observed that an increase in solidity generally increases the velocity roughness function, but the roughness function is comparable for the

medium and the high solidity. The previously observed behaviour of a decrease in velocity roughness function above a threshold solidity of $\Lambda = 0.18$ is only seen for low roughness height of $k^+ \approx 11$. In case of temperature, an increase in roughness function with solidity is observed, with each individual solidity set tending towards a constant of its own.

Instantaneous velocity and temperature contours show thin sublayers near the wall for low roughness heights, submerging the roughness elements. With an increased roughness height, recirculation regions get larger within the roughness canopy, while the thermal sublayer slowly starts conforming to the shape of the roughness elements. Total volume of the fluid within the recirculation region is calculated and compared to the total volume of the fluid under the roughness crest, and an increase in this ratio for increasing roughness solidity was observed. An increased recirculation region is most likely facilitating the exchange of well-mixed fluid from outside the thermal sublayer. This, along with the increase in wetted area for increasing solidity, may explain the increase in heat transfer for higher solidity.

Bibliography

Abe, H., Kawamura, H. & Matsuo, Y. 2001 Direct numerical simulation of a fully developed turbulent channel flow with respect to the reynolds number dependence. *Journal of Fluids Engineering* **123** (2), 382–393.

Abe, H., Kawamura, H. & Matsuo, Y. 2004 Surface heat-flux fluctuations in a turbulent channel flow up to $Re_\tau = 1020$ with $Pr = 0.025$ and 0.71. *International Journal of Heat and Fluid Flow* **25** (3), 404–419.

Bernardini, M., Pirozzoli, S. & Orlandi, P. 2014 Velocity statistics in turbulent channel flow up to $Re_\tau = 4000$. *Journal of Fluid Mechanics* **742**, 171–191.

Busse, A., Thakkar, M. & Sandham, N. D. 2017 Reynolds-number dependence of the near-wall flow over irregular rough surfaces. *Journal of Fluid Mechanics* **810**, 196–224.

Cebeci, T. & Bradshaw, P. 1984 *Physical and Computational Aspects of Convective Heat Transfer*. Springer.

Çengel, Y. A. & Cimbala, J. M. 2018 *Fluid Mechanics*. McGraw-Hill Education.

Chan, L., MacDonald, M., Chung, D., Hutchins, N. & Ooi, A. 2015 A systematic investigation of roughness height and wavelength in turbulent pipe flow in the transitionally rough regime. *Journal of Fluid Mechanics* **771**, 743–777.

Chan, L., MacDonald, M., Chung, D., Hutchins, N. & Ooi, A. 2018 Secondary motion in turbulent pipe flow with three-dimensional roughness. *Journal of Fluid Mechanics* **854**, 5–33.

Chung, D., Chan, L., MacDonald, M., Hutchins, N. & Ooi, A. 2015 A fast direct numerical simulation method for characterising hydraulic roughness. *Journal of Fluid Mechanics* **773**, 418–431.

Chung, D., Monty, J. P. & Ooi, A. 2014 An idealised assessment of Townsend's outer-layer similarity hypothesis for wall turbulence. *Journal of Fluid Mechanics* **742**, R3.

Colebrook, C. F. 1939 Turbulent flow in pipes, with particular reference to the transition region between the smooth and rough pipe laws. *Journal of the Institution of Civil Engineers* **11** (4), 133–156.

Coleman, Gary N. & Sandberg, Richard D. 2010 A primer on direct numerical simulation of turbulence - methods, procedures and guidelines. Project report. University of Southampton.

Coles, D. 1956 The law of the wake in the turbulent boundary layer. *Journal of Fluid Mechanics* **1** (2), 191–226.

Cope, W. F. 1941 The friction and heat transmission coefficients of rough pipes. *Proceedings of the Institution of Mechanical Engineers* **145** (1), 99–105.

Dipprey, D. F. & Sabersky, R. H. 1963 Heat and momentum transfer in smooth and rough tubes at various prandtl numbers. *International Journal of Heat and Mass Transfer* **6** (5), 329–353.

Fadlun, E. A., Verzicco, R., Orlandi, P. & Mohd-Yusof, J. 2000 Combined immersed-boundary finite-difference methods for three-dimensional complex flow simulations. *Journal of Computational Physics* **161** (1), 35–60.

Flack, K. A. 2018 Moving beyond moody. *Journal of Fluid Mechanics* **842**, 1–4.

Flack, K. A. & Schultz, M. P. 2010 Review of hydraulic roughness scales in the fully rough regime. *Journal of Fluids Engineering* **132**, 041203.

Flack, K. A. & Schultz, M. P. 2014 Roughness effects on wall-bounded turbulent flows. *Physics of Fluids* **26** (10), 101305.

Forooghi, P., Stripf, M. & Frohnapfel, B. 2018 A systematic study of turbulent heat transfer over rough walls. *International Journal of Heat and Mass Transfer* **127**, 1157–1168.

Grimmond, C. S. B. & Oke, T. R. 1999 Aerodynamic properties of urban areas derived from analysis of surface form. *Journal of Applied Meteorology* **38** (9), 1262–1292.

Hama, F. R. 1954 Boundary layer characteristics for smooth and rough surfaces. *Transactions of the Society of Naval Architects and Marine Engineers* **62**, 333–358.

Jiménez, J. 2004 Turbulent flows over rough walls. *Annual Review of Fluid Mechanics* **36** (1), 173–196.

Kader, B. A. 1981 Temperature and concentration profiles in fully turbulent boundary layers. *International Journal of Heat and Mass Transfer* **24** (9), 1541–1544.

von Kármán, T. 1930 Mechanische ähnlichkeit und Turbulenz. *Nachrichten von der Gesellschaft der Wissenschaften zu Göttingen : Mathematisch-physische Klasse* pp. 58–76.

Kawamura, H., Ohsaka, K., Abe, H. & Yamamoto, K. 1998 DNS of turbulent heat transfer in channel flow with low to medium-high prandtl number fluid. *International Journal of Heat and Fluid Flow* **19** (5), 482–491.

Kozuka, M., Seki, Y. & Kawamura, H. 2009 DNS of turbulent heat transfer in a channel flow with a high spatial resolution. *International Journal of Heat and Fluid Flow* **30** (3), 514–524.

Leonardi, S., Orlandi, P., Djenidi, L. & Antonia, R. A. 2015 Heat transfer in a turbulent channel flow with square bars or circular rods on one wall. *Journal of Fluid Mechanics* **776**, 512–530.

Lozano-Durán, A. & Jiménez, J. 2014 Effect of the computational domain on direct simulations of turbulent channels up to $Re_\tau = 4200$. *Physics of Fluids* **26** (1), 011702.

Luchini, P., Manzo, F. & Pozzi, A. 1991 Resistance of a grooved surface to parallel flow and cross-flow. *Journal of Fluid Mechanics* **228**, 87–109.

MacDonald, M., Chan, L., Chung, D., Hutchins, N. & Ooi, A. 2016 Turbulent flow over transitionally rough surfaces with varying roughness densities. *Journal of Fluid Mechanics* **804**, 130–161.

MacDonald, M., Hutchins, N. & Chung, D. 2019 Roughness effects in turbulent forced convection. *Journal of Fluid Mechanics* **861**, 138–162.

Marusic, I., Monty, J. P., Hultmark, M. & Smits, A. J. 2013 On the logarithmic region in wall turbulence. *Journal of Fluid Mechanics* **716**, R3.

Milikan, C. B. 1938 A critical discussion of turbulent flows in channels and circular tubes. *Proceedings of the Fifth International Congress for Applied Mechanics* pp. 386–392.

Miyake, Y., Tsujimoto, K. & Nakaji, M. 2001 Direct numerical simulation of rough-wall heat transfer in a turbulent channel flow. *International Journal of Heat and Fluid Flow* **22** (3), 237–244.

Moody, L. F. 1944 Friction factors for pipe flow. *Trans. ASME* **66**, 671–684.

Moser, R. D., Kim, J. & Mansour, N. N. 1999 Direct numerical simulation of turbulent channel flow up to $Re_\tau = 590$. *Physics of Fluids* **11**, 943–945.

Musker, A. J. 1980 Universal roughness functions for naturally-occurring surfaces. *Transactions of the Canadian Society for Mechanical Engineering* **6** (1), 1–6.

Nagib, H. & Chauhan, K. 2008 Variations of von Kármán coefficient in canonical flows. *Physics of Fluids* **20**.

Napoli, E., Armenio, V. & De Marchis, M. 2008 The effect of the slope of irregularly distributed roughness elements on turbulent wall-bounded flows. *Journal of Fluid Mechanics* **613**, 385–394.

Nikuradse, J. 1933 Laws of flow in rough pipes. *VDI Forschungsheft* p. 361.

Nunner, W. & Hudswell, F. 1958 *Heat Transfer and Pressure Drop in Rough Tubes*. Atomic Energy Research Establishment.

Owen, P. R. & Thomson, W. R. 1963 Heat transfer across rough surfaces. *Journal of Fluid Mechanics* **15** (3), 321–334.

Perot, J. B. 1993 An analysis of the fractional step method. *Journal of Computational Physics* **108** (1), 51–58.

Pirozzoli, S., Bernardini, M. & Orlandi, P. 2016 Passive scalars in turbulent channel flow at high Reynolds number. *Journal of Fluid Mechanics* **788**, 614–639.

Placidi, M. & Ganapathisubramani, B. 2015 Effects of frontal and plan solidities on aerodynamic parameters and the roughness sublayer in turbulent boundary layers. *Journal of Fluid Mechanics* **782**, 541–566.

Pope, S. B. 2000 *Turbulent Flows*. Cambridge University Press.

Prandtl, L. 1925 Bericht über Untersuchungen zur ausgebildeten Turbulenz. *Zeitschrift für Angewandte Mathematik und Mechanik* **5** (2), 136–139.

Raupach, M. R., A. Antonia, R. & Rajagopalan, S. 1991 Rough-wall turbulent boundary layers. *Applied Mechanics Reviews* **44**, 1–25.

Raupach, M. R. & Shaw, R. H. 1982 Averaging procedures for flow within vegetation canopies. *Boundary-Layer Meteorology* **22** (1), 79–90.

Reynolds, O. 1883 XXIX. An experimental investigation of the circumstances which determine whether the motion of water shall be direct or sinuous, and of the law of resistance in parallel channels. *Philosophical Transactions of the Royal Society of London* **174**, 935–982.

Rouhi, A., Chung, D. & Hutchins, N. 2019 Direct numerical simulation of open-channel flow over smooth-to-rough and rough-to-smooth step changes. *Journal of Fluid Mechanics* **866**, 450–486.

Schlichting, H. 1936 Experimental investigation of the problem of surface roughness. *Ingenieur–Archiv* **7**, 1–34.

Schultz, M. P., Bendick, J. A., Holm, E. R. & Hertel, W. M. 2011 Economic impact of biofouling on a naval surface ship. *Biofouling* **27** (1), 87–98.

Schultz, M. P. & Flack, K. A. 2009 Turbulent boundary layers on a systematically varied rough wall. *Physics of Fluids* **21** (1), 015104.

Scotti, A. 2006 Direct numerical simulation of turbulent channel flows with boundary roughened with virtual sandpaper. *Physics of Fluids* **18** (3), 031701.

Spalart, P. R., Moser, R. D. & Rogers, M. R. 1991 Spectral methods for the navier–stokes equations with one infinite and two periodic directions. *Journal of Computational Physics* **96** (2), 297–324.

Tennekes, H. & Lumley, J. 1972 *A First Course in Turbulence*. MIT Press.

Thom, A. S. 1971 Momentum absorption by vegetation. *Quarterly Journal of the Royal Meteorological Society* **97**, 414–428.

Townsend, A. A. 1976 *The Structure of Turbulent Shear Flow*, 2nd edn. Cambridge University Press.

Verstappen, R. W. C. P. & Veldman, A. E. P. 2003 Symmetry-preserving discretization of turbulent flow. *Journal of Computational Physics* **187** (1), 343–368.

Webb, R. L. & Eckert, E. R. G. 1972 Application of rough surfaces to heat exchanger design. *International Journal of Heat and Mass Transfer* **15** (9), 1647–1658.

Yaglom, A. M. 1979 Similarity laws for constant-pressure and pressure-gradient turbulent wall flows. *Annual Review of Fluid Mechanics* **11** (1), 505–540.

Yang, D., Meneveau, C. & Shen, L. 2013 Dynamic modelling of sea-surface roughness for large-eddy simulation of wind over ocean wavefield. *Journal of Fluid Mechanics* **726**, 62–99.

Yuan, J. & Piomelli, U. 2014 Numerical simulations of sink-flow boundary layers over rough surfaces. *Physics of Fluids* **26** (1), 015113.